An Enhanced Deep-Learning Catalog of the Mw 8.8 Maule Aftershock Sequence

Rodrigo Flores-Allende[1], Léonard Seydoux[1], Éric Beaucé[2,3], Luis Fabian Bonilla[3,1], Philippe Gueguen[4] and Claudio Satriano[1]

[1]Université Paris Cité, Institut de physique du globe de Paris, UMR 7154, Paris, France
[2]Lamont-Doherty Earth Observatory, Columbia University, New York, NY, USA
[3]Université Gustave Eiffel, Champs-sur-Marne, Marne-la-Vallée, France
[4]ISTerre, Université Grenoble Alpes/CNRS/Univ. Savoie Mont-Blanc/IRD/Université Gustave Eiffel, 38000 Grenoble, France

Corresponding author: floresallende@ipgp.fr

An Enhanced Deep-Learning Catalog of the M_{w} 8.8 Maule Aftershock Sequence

Rodrigo Flores-Allende[1], Léonard Seydoux[1], Éric Beaucé[2], Luis Fabian Bonilla[3,1], Philippe Gueguen[4] and Claudio Satriano[1]

[1]Université Paris Cité, Institut de physique du globe de Paris, UMR 7154, Paris, France
[2]Lamont-Doherty Earth Observatory, Columbia University, New York, NY, USA
[3]Université Gustave Eiffel, Champs-sur-Marne, Marne-la-Vallée, France
[4]ISTerre, Université Grenoble Alpes/CNRS/Univ. Savoie Mont-Blanc/IRD/Université Gustave Eiffel, 38000 Grenoble, France

Key Points:

- Improved catalog of the M_{w} 8.8 Maule earthquake aftershock sequence over 10 months.
- Deep-learning workflow for detection, location, relocation, and magnitude estimation.
- Increase of ca. 12 times the number of detections compared to previous catalogs.
- Spatial b-value patterns suggest fault segmentation and along-strike variations in stress and fluid conditions.

Corresponding author: Rodrigo Flores-Allende, `floresallende@ipgp.fr`

Abstract

We re-examine the aftershock sequence of the M_w 8.8 Maule earthquake in south-central Chile using deep-learning on 10 months of continuous seismic data from 156 temporary stations along the rupture zone (March 2010—March 2011). By integrating back-projection and matched filtering with PhaseNet (a deep-learning phase picker), we initially identify 99,137 earthquakes. We then relocate these events using NonLinLoc with source-specific station terms and waveform coherence. We select a subset of 8,930 earthquakes for template matching and obtain a final catalog of 374,058 earthquakes —nearly 12 times more than previous studies— achieving a magnitude of completeness of M_w 1.7, which is an order of magnitude lower. The spatiotemporal evolution of the seismicity reveals intricate seismic structures, including a highly active shallow cluster in the Pichilemu-Vichuquén region (33.5°S–35°S) showing a complex L-shaped geometry and deeper slab-related seismicity near Concepción (37°S–38°S). Spatial and temporal variation of the *b*-value further highlight heterogeneous post-seismic deformation driven by multiple fault system activations. This study demonstrates how modern analytical techniques, particularly machine learning, extract valuable insights from older datasets, enabling the discovery of previously undetected small-amplitude seismicity and refining our understanding of earthquake dynamics and seismic hazards.

Plain Language Summary

After a large earthquake, understanding how the Earth's crust adjusts is crucial for improving seismic hazard assessments. Seismologists study these processes using earthquake catalogs, which document the timing, location, and magnitude of recorded events. Both large and small earthquakes provide valuable insights into the physical processes at play within the crust, as their relative distribution reflects underlying stress and deformation mechanisms. However, the quality of catalogs depends on how well earthquakes can be detected, located, and measured. Small-magnitude events, in particular, are more challenging to identify due to background noise and variations in data quality. This study enhances the aftershock catalog of the 2010 M_w 8.8 Maule earthquake in south-central Chile by analyzing 10 months of continuous seismic data from 156 temporary stations. By applying modern techniques, including artificial intelligence and machine learning, we identify over 375,000 earthquakes—nearly 12 times more than previous catalogs. The expanded catalog provides a significantly more detailed view of aftershock distribution, revealing complex seismic patterns. It highlights shallow activity primarily associated with crustal faults and deeper seismicity linked to the subducting slab. We also examine the *b*-value, which quantifies the ratio of large to small earthquakes. Variations in the *b*-value offer key insights into how stress evolves over space and time, suggesting a combination of processes driving post-seismic deformation. Our study demonstrates how modern computational techniques can extract valuable information from historical seismic datasets. By constructing more detailed earthquake catalogs, these methods improve our understanding of seismicity and contribute to better earthquake hazard assessments.

1 Introduction

On February 27, 2010, a M_w 8.8 earthquake struck the Maule region in central-south Chile, causing significant loss of life and widespread damage (Salazar & McNutt, 2011). The rupture extended 500 km along the convergence margin between the Pacific and Nazca plates, between latitudes 33°S and 38.5°S (Figure 1a). This event ranks among the largest instrumentally recorded earthquakes worldwide, and is the strongest well-recorded in Chile (e.g., Delouis et al., 2010; Madariaga et al., 2010; Moreno et al., 2010; Vigny et al., 2011; S. Ruiz et al., 2012; Hicks et al., 2014; S. Ruiz & Madariaga, 2018). Its rupture coincides with the mature seismic gap left by the M_w 8.3 earthquake of 1835 (see e.g., Campos et al., 2002), and overlaps segments of previous major earthquakes, including the M_w 7.7 Talca (1928), M_w 8.1 Concepción (1960, e.g., Ojeda et al., 2020), and M_w 7.8 Arauco (1975) earthquakes.

It also partially overlaps the M_w 9.5 Valdivia earthquake area of 1960, the largest earthquake ever recorded in history (e.g., Madariaga et al., 2010; S. Ruiz et al., 2012).

Large megathrust earthquakes, such as those related to subduction zones, are typically followed by an increase in seismic activity known as aftershocks. Earthquakes are considered aftershocks when their magnitude is at least one unit smaller than the mainshock (Båth, 1965), and can persist for weeks to years (Bilek & Lay, 2018). They result from stress perturbations induced by the main rupture (Felzer et al., 2004), and their distribution across the rupture zone often correlates with regions of high post-seismic strain and substantial static stress changes (Lange et al., 2012; Rietbrock et al., 2012). Among the many aftershocks of the Maule earthquake, shortly after the mainshock, two large aftershocks of M_w 6.9 and M_w 6.7 struck the area of Pichilemu on March 11, 2010, at the northern edge of the rupture zone (Farías et al., 2011; Lange et al., 2012; Rietbrock et al., 2012; Ryder et al., 2012; J. A. Ruiz et al., 2014). These aftershocks suggest a potential migration of seismicity or the reactivation of analogous fault systems in the region.

Over the past decade, the International Maule Aftershock Deployment (IMAD) dataset has been a key resource for studying the Maule aftershock sequence. Deployed within a few weeks after the mainshock, this mobile seismic network covered the entire rupture area (Figure 1a) and enabled the construction of some early earthquake catalogs. For instance, Lange et al. (2012) and Rietbrock et al. (2012) applied classical Short-Term Average to Long-Term Average (STA/LTA) automatic pickers, detecting over 20,000 events in six months and more than 30,000 events in just two months, respectively. These initial efforts provided a broad overview of the rupture segmentation, aftershock distribution, and fault reactivation. Using the catalog from Rietbrock et al. (2012), Agurto et al. (2012) refined the locations of the largest aftershocks and performed regional moment tensor (RMT) inversions to characterize spatio-temporal variations in seismic moment release. One of the main observations was the apparent lack of large aftershocks in regions of highest coseismic slip (Agurto et al., 2012; Rietbrock et al., 2012). Although this pattern appears to depend on the selected slip model, both studies agreed that only low-magnitude seismicity was present in these high-slip patches. This emphasizes the need for accurate detection and location of small events to delineate and characterize the interaction between seismic and aseismic patches. As a result, the contribution of these regions to the total postseismic deformation budget remains unclear, and deeper intraslab contributions may also be underestimated. Moreover, Tassara et al. (2016) analyzed b-value patterns in relation to afterslip and identified contrasting mechanical domains along strike, likely controlled by variations in fluid content and fault rheology. Similarly, Neighbors et al. (2015) estimated the high-frequency attenuation parameter κ, finding significant spatial variability likely reflecting the combined effects of source, path, and site conditions, though poorly correlated with surface geology. While both studies provided valuable insights, their resolution was limited by the number of events used, as they considered only a few subsets of moderate-to-large magnitude aftershocks.

A clear understanding of aftershock patterns, afterslip distribution, and triggering mechanisms is key to improving our knowledge of earthquake mechanics (Peng & Zhao, 2009; Yao et al., 2017; Minetto et al., 2022; Farge & Brodsky, 2025). Although often neglected in stress-transfer models, small-magnitude earthquakes can collectively have a significant impact due to their high ocurrence and spatial clustering. Marsan (2005) demonstrated that stress perturbations from small earthquakes can be as influential as those from larger ones, highlighting the importance of including microseismicity in further analysis. For instance, S. Ruiz et al. (2017) used repeaters to reveal aseismic processes before and after the 2017 M_w 6.9 Valparaiso earthquake, suggesting that small-scale seismicity may have triggered the mainshock and played an important role in the rupture dynamics. However, current studies mainly rely on large-magnitude aftershocks, as detecting smaller ones remains challenging. Seismic noise often hinders the detection of low-magnitude aftershocks, particularly when using traditional methods based on signal amplitude such as Signal-to-Noise Ratio (SNR) or the previously mentioned STA/LTA trigger (see e.g., Allen, 1982).

Other factors, such as wave scattering and attenuation, further complicate the detection of small aftershocks, especially in regions with extensive rupture zones and sparse seismic networks like in the present study (Figure 1b).

Recent advances in deep learning have significantly improved the quality of earthquake catalogs (Ross et al., 2019; Mousavi & Beroza, 2023; Zhu & Beroza, 2019). These methods excel at identifying low-magnitude events and provide more reliable locations, unveiling the intricate details of seismic sequences and fault structures (Beaucé et al., 2019; Tan et al., 2021; Beaucé et al., 2022; Mancini et al., 2022; Minetto et al., 2022). In this study, we use these techniques to reassess an old, but distinctive dataset recorded by the IMAD network (Beck et al., 2014). We present a high-resolution earthquake catalog of the Maule aftershock sequence and a spatiotemporal analysis of the seismicity. Our aim is to uncover previously unresolved features related to the rupture dynamics during the aftershock sequence of the Maule earthquake over a 10 month period. The strategy is based on Beaucé et al. (2024), a deep-neural-network automatic seismic phase picking (Zhu & Beroza, 2019) associated in space with backprojection (Frank & Shapiro, 2014) to detect and locate earthquakes and two relocation stages (Lomax, 2001; Lomax & Savvaidis, 2022) to build an initial catalog. Subsequently, we apply a template matching with the detected events (Gibbons & Ringdal, 2006; Frank & Shapiro, 2014; Beaucé et al., 2018) to identify new earthquakes, which may otherwise be missed by conventional techniques, thus increasing the catalog resolution (Minetto et al., 2022).

In the following sections, we first outline the tectonic context of central-south Chile, with a focus on the 2010 Maule earthquake and its aftershock sequence. We then introduce the IMAD database and the BeamPower and Matched-Filtering (BPMF, Beaucé et al., 2024) method used for earthquake detection and location, applying this approach to nearly 10 months of seismic data covering the entire rupture zone. Next, we detect, locate, and relocate events based on the quality of automatic picks, estimate moment magnitudes, and perform a Gutenberg-Richter analysis, including new methods for calculating the b-value. Finally, we analyze the spatiotemporal distribution of seismicity in the catalog and compare it with previous catalogs to assess improvements in catalog resolution.

2 Geotectonic setting

The Maule segment of the south-central Chilean subduction zone (33°-39°S) is a tectonically transitional region that accommodates oblique convergence between the Nazca and South American plates at approximately 66 mm/year (Haberland et al., 2009). This segment is bounded by the subducted Juan Fernández Ridge to the north and the Mocha Fracture Zone to the south, and marks a transition from a strongly coupled interface in central Chile to a more weakly coupled regime farther south (Moreno et al., 2010; Vigny et al., 2011). The segmentation is shaped by inherited lithospheric discontinuities, including the Lanalhue Fault Zone and terrane boundaries across a metamorphic Paleozoic basement intruded by Mesozoic granitoids (Hervé et al., 1987, 1988; Mpodozis & Ramos, 1990; Glodny et al., 2008; Aron et al., 2015). These crustal features influence upper-plate faulting, forearc uplift, and variations in mechanical coupling (Melnick et al., 2009). This geotectonically complex segment ruptured during the $M_{\mathrm{w}}\,8.8$ mainshock and is believed to have released the strain accumulated since 1835 (Campos et al., 2002; Ruegg et al., 2009). The rupture nucleated near 36.5°S and propagated bilaterally, producing two major slip patches, a northern one with a peak up to 20 m, overlapping the probable 1928 rupture zone and extending north toward the 1985 rupture border, and a southern one, with approximately 10 m of slip overlapping the northern edge of the 1960 $M_{\mathrm{w}}\,9.5$ rupture zone (Figure 1a; Delouis et al., 2010; Lorito et al., 2011; Pollitz et al., 2011; S. Ruiz et al., 2012; Yue et al., 2014). Despite its magnitude, the Maule earthquake may not have fully released all the accumulated stress (Madariaga et al., 2010; Moreno et al., 2010), underscoring the role of margin segmentation and structural inheritance in governing rupture propagation and seismic potential.

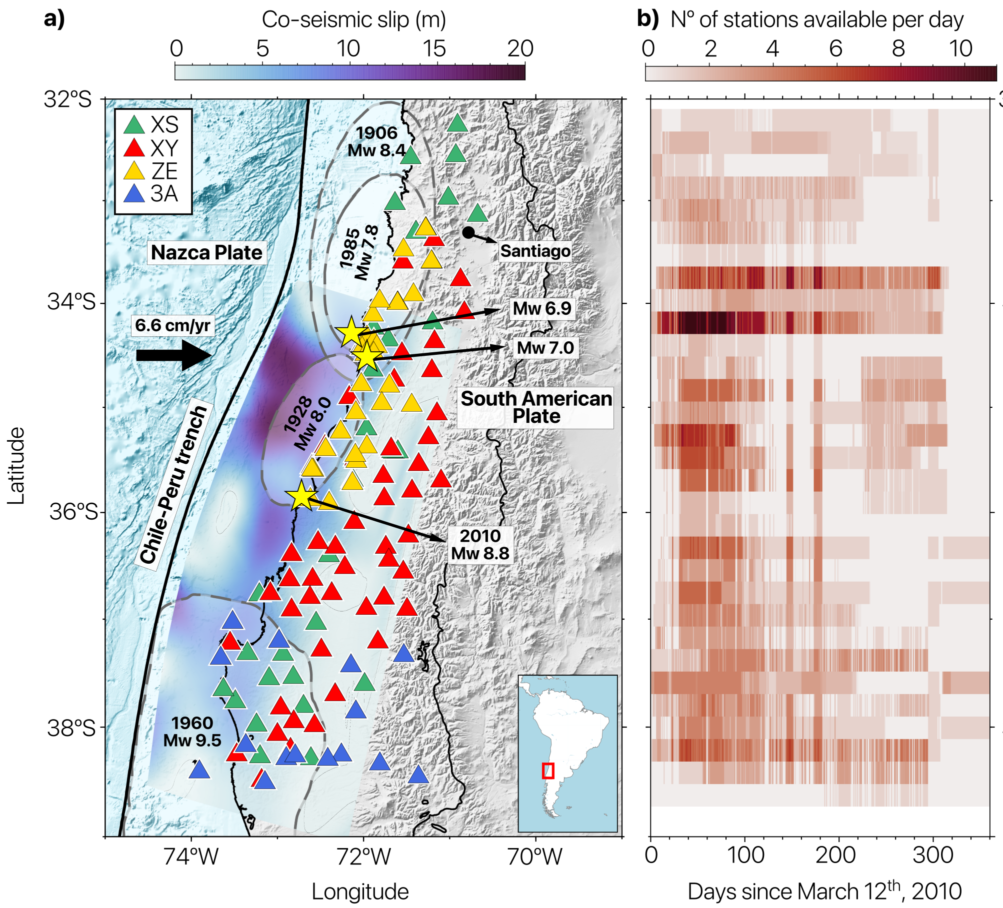

Figure 1. **Study area and data coverage.** **(a)** Seismic stations deployed in south-central Chile after the mainshock (triangles). Each color represents a network managed by different institutions: RESIF (XS in green, Vilotte & et al., 2011), University of Florida (XY in red Steve Roecker & Ray Russo, 2010), GFZ (ZE in yellow), and University of Liverpool (3A in blue, Beck et al., 2014). The coseismic slip model presented by (Yue et al., 2014) is represented in background colors, with darker zones related to larger slip. The yellow star marks the location of the M_w 8.8 mainshock on February 27, 2010, as well as the largest aftershocks in the Pichilemu zone (34°30'S), with magnitudes M_w 6.9 and M_w 7.0, respectively. Historical rupture areas are depicted with gray ellipses. **(b)** Spatiotemporal availability of data. The color indicates the daily density of stations available every 0.2° of latitude.

3 Data and Methods

We retrieve one year of seismic data from the IMAD dataset, which records a post-seismic mobile network operated by France, the United States, Germany, the United Kingdom, and collaborating partners, covering from March 2010 to March 2011 (see e.g., Beck et al., 2014). This seismic array included nearly 156 instruments equipped with accelerometers, short-period seismometers, and broadband seismometers (Figure 1a). Stations were deployed across the entire rupture area (Figure 1a), though not all operated simultaneously or for the same durations (Figure 1b). Also, external conditions caused fluctuations in station availability over time, making the dataset less stable and uniform (Lange et al., 2012), so that at certain periods, fewer than 20 stations were operational, while at maximum, nearly 120 stations were simultaneously active.

To mitigate this variability, we exclude stations and traces with substantial data gaps. In regions with multiple stations within a 500 m radius, we select one station to avoid redundancy. Finally, we focus on periods with consistent availability of at least five stations, defined as the lowest threshold providing sufficient spatial and temporal coverage. This minimum threshold does not vary across the study area or over time, although the specific station combinations may change depending on the variable network configuration. The sequential steps of the workflow are illustrated in Figure 2, with further details provided in the subsequent sections. This workflow is based on the BPMF algorithm (Beaucé et al., 2024) which outputs are post-processed with NonLinLoc-SSST-Coherence (Lomax & Savvaidis, 2022) to enhance earthquake locations, and SourceSpec to estimate the moment magnitudes (Satriano, 2021). These tools complement the original framework, and were included to increase the robustness of the results.

3.1 Seismogram preparation

We first bandpass-filter the continuous data within 1 and 12 Hz to discard low-frequency noise. We select this frequency range from an initial visual inspection of the data, which show energy concentrations mainly above 1 Hz. This approach is consistent with the parameters applied by Cabrera et al. (2021) in a similar tectonic context. Furthermore, we resample the data to a sampling rate of 25 Hz to reduce computational costs without compromising the efficiency of our analysis, giving a good balance between preserving the frequency content of local earthquakes and suppressing unwanted noise. In addition, we ensure the inclusion of only stations with minimal data gaps and consistent operational records. We include data segments if they met two key criteria: (1) a minimum total duration of 75 % of the expected recording period for the event or station, ensuring sufficient temporal coverage despite potential gaps, and (2) individual contiguous chunks with a duration of at least 600 s, excluding excessively short fragments unsuitable for the analysis.

3.2 Initial earthquake detection and location

To detect and locate the initial earthquakes, we build a 3D spatial grid of potential point sources (Figure 3a). The grid covers the full extent of the rupture area, with a horizontal spacing of 0.03° in both latitude and longitude, and a vertical spacing of 0.5 km, reaching depths up to 100 km. We calculate the travel time of P and S waves for each tested source withing a 1D velocity model for South-Central Chile (Hicks et al., 2014) adapted to include the slab geometry from the Slab 2.0 model (Hayes, 2018), as presented in Figure S1 from the Supporting Information. We also apply a Gaussian smoothing filter to minimize abrupt velocity changes between layers, reducing artifacts in earthquake locations. This approach accounts for finite-frequency effects and prevents the formation of guided waves at sharp velocity discontinuities.

We compute the travel times (or moveouts) τ_{sk}^{ϕ} from each point source k to every station s for the seismic phase $\phi \in \{P, S\}$ by solving the eikonal equation (White et al., 2020). We

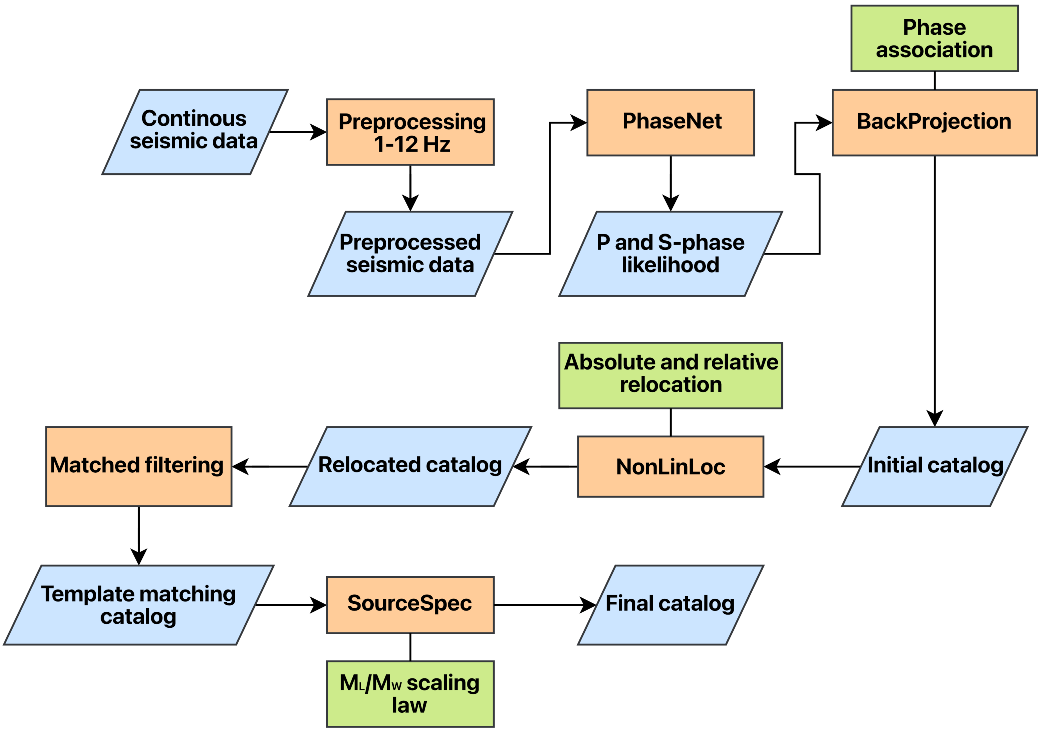

Figure 2. Earthquake catalog workflow. Blue boxes represent data (inputs or outputs), orange boxes indicate operations, and green boxes highlight some key steps. Continuous seismic data are filtered between 1 and 12 Hz and processed with PhaseNet to identify P and S-phase likelihoods. We associate the phases in space with backprojection to detect and locate the initial events, and relocate them with NonLinLoc. Additional techniques, such as template matching, contribute to increase the catalog completeness, while SourceSpec enables the magnitude estimation.

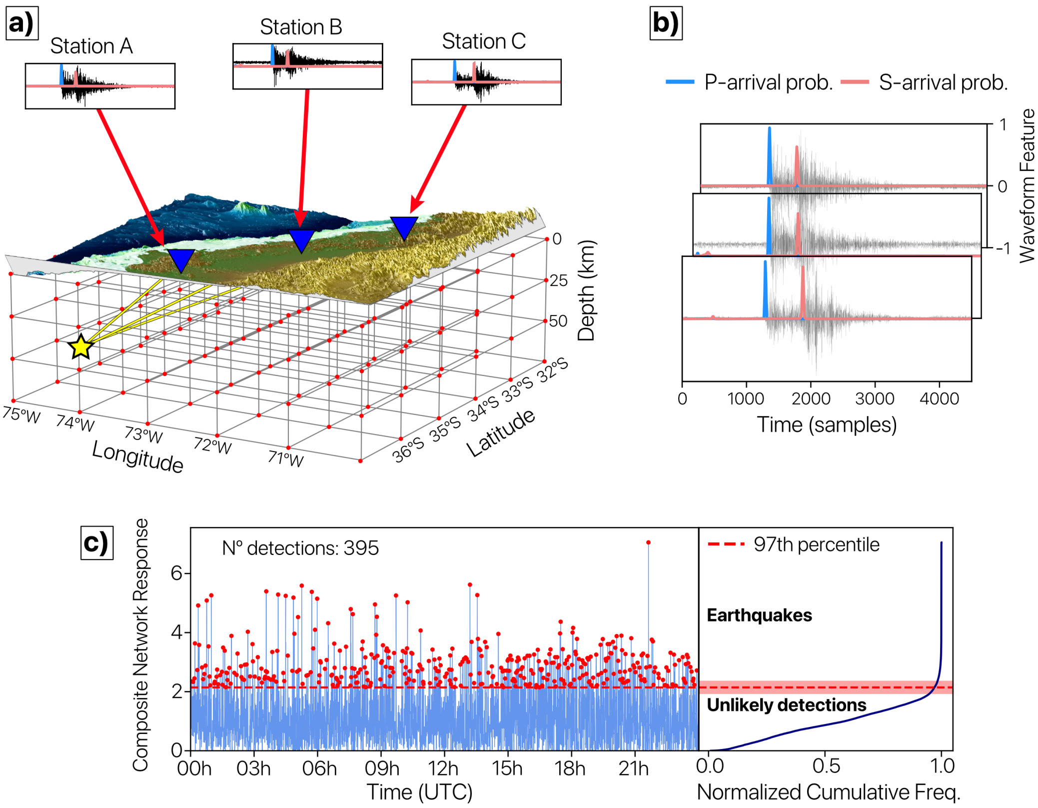

Figure 3. Earthquake detection and initial location. **(a)** Illustration of the grid with tested source points. The yellow star indicates the true earthquake location, with corresponding signals recorded at the seismic stations. **(b)** Example seismic record with the *P* and *S* likelihoods obtained using PhaseNet (Zhu & Beroza, 2019, respectively in blue and orange). **(c)** Composite network response obtained by shifting and stacking the waveform features for each component and station over time (Beaucé et al., 2024). The detection threshold is indicated with a dashed red line, with red points indicating events interpreted as localized sources.

use the deep learning automatic phase picking algorithm PhaseNet (Zhu & Beroza, 2019) to estimate the probabilities $\nu_{s\phi}(t)$ of P- and S-wave arrivals in continuous seismic data (as illustrated in Figures 3b, and S2). Next, we delay $\nu_{s\phi}(t)$ according to the computed moveouts and stack the waveform features to identify the most likely source location. This serves as an efficient seismic phase association mechanism (see also Figure 3b). The stacked response, also named beamforming by Frank and Shapiro (2014), is defined as:

$$b_k(t) = \sum_{s\in\mathcal{S}_k} \sum_{\phi\in\{P,S\}} \nu_{s\phi}\left(t + \tau_{sk}^{\phi}\right). \tag{1}$$

Coherent seismic signals produce higher values of $b_k(t)$ when aligned with a likely source k, whereas incoherent noise does not contribute constructively. The set of seismic stations $\mathcal{S}_k$ only considers the ten closes stations to the source k to enhance source-to-station sensitivity. The final source location is determined by identifying the maximum value of the composite network response (CNR) defined as the beamforming maximum over time $\mathcal{B}(t) = \max_k b_k(t)$.

The CNR allows the detection and location of earthquakes with increased sensitivity and precision (Beaucé et al., 2019, 2022, 2024). It provides an initial estimate of the event location by identifying the time at which the beam power reaches its peak. However, the accuracy of this location strongly depends on the grid resolution and the velocity model. A finer grid, with more potential source points k, improves spatial precision but drastically increases computational cost. A key challenge in this process is to distinguish between beams corresponding to real earthquakes and those resulting from noise, unlikely signals or artifacts. Finally, given the large study area and the heterogeneous station coverage, the stacked signal response varies over time, making the choice of a detection threshold non-trivial. To address this, we implement a dynamic threshold approach based on the cumulative distribution function of the daily CNR. Assuming that most low-amplitude beams do not correspond to real events, we define the threshold at the inflection point, or “knee”, of the distribution (Figure 3c). However, in cases where the knee is not well-defined, we are aware that the uncertainty in event detection could increases.

To maintain a conservative yet effective detection criterion, we set the threshold at the 97^{th} percentile of the beam power distribution. We also note that values between the 95^{th} and 99^{th} percentiles can effectively distinguish potential seismic signals while reducing the likelihood of false detections. This adaptive approach ensures that the detection threshold dynamically adjusts to the empirical characteristics of the dataset, optimizing the balance between sensitivity and reliability.

3.3 Initial events relocation

As previously mentioned, the initial backprojection is highly sensitive to the spatial resolution of the 3D grid and the velocity model. To improve location accuracy, we employ the NonLinLoc-SSST-Coherence algorithm (Lomax, 2001; Lomax et al., 2009; Lomax & Savvaidis, 2022), which refines event locations using probabilistic inversion methods while accounting for uncertainties.

NonLinLoc uses the *a priori* P- and S-wave picks identified by PhaseNet, to perform a grid search and sample the likelihood of hypocenter locations (Figure S3). We also apply Source-Specific Station Term (SSST) corrections, which iteratively refine travel-time estimates by minimizing residuals between observed and predicted seismic phase arrivals (Figure S4). This approach accounts for spatial velocity variations, producing a smoother station-specific velocity model and allowing travel-time corrections to adapt to regional heterogeneities, resulting in more precise and well-clustered earthquake locations. However, the S-phase residuals show a consistently positive trend across stations (Figure S4), suggesting a systematic bias in the travel-time predictions likely caused by limitations in the regional velocity model. While SSST corrections help mitigate local anomalies, further improvements could be achieved by integrating higher-resolution 3D tomographic models.

Finally, we apply a relative relocation method based on waveform coherence (Lomax & Savvaidis, 2022), conceptually similar to other techniques such as HypoDD (Waldhauser, 2001) or GrowClust (Trugman & Shearer, 2017), but without relying on differential travel times. High waveform coherence, quantified by the maximum cross-correlation, suggests that close events originate from nearby sources. We stack the location PDFs of highly correlated events and relocate them within their shared probability region. This approach enhances location accuracy, even in regions with sparse station coverage and limited datasets, such as in our case.

3.4 Template matching

Template matching is a technique to identify new earthquakes with a low signal-to-noise ratio from existing templates(Anstey, 1964; Gibbons & Ringdal, 2006; Shelly et al., 2007; Frank & Shapiro, 2014; Skoumal et al., 2014; Beaucé et al., 2018; Cabrera et al., 2021; Beaucé et al., 2022; Minetto et al., 2022). This process quantifies the similarity between seismic waveforms, triggering a new detection when the correlation is sufficiently high (Figure S5). We define as templates a subset of earthquakes with location uncertainties below 10 km of hypocentral distance. To avoid redundancy, which could result in multiple detections of the same earthquake, we group highly correlated templates (more than 0.5 correlation coefficient) and we select the event which has the lowest combined horizontal and vertical uncertainty among them. Each template consists of a 10 s signal window, focusing on the P-wave phase in the vertical component and the S-wave phase in the horizontal components.

We finally cross-correlate the continuous data with the templates in search for high correlation values. New detections are identified when the cross-correlation coefficient exceeds a time-dependent threshold, calculated as 8 times the Root Mean Square (RMS) of each 30 min segments, which consistent with conservative thresholds used in previous template matching studies (e.g., Shelly et al., 2007; Ross et al., 2019; Beaucé et al., 2022). We require a minimum of three available stations and six channels to trigger a new detection, based on the network-averaged cross-correlation coefficient, and limit the search to a maximum of ten stations per template, selected based on proximity, to optimize performance in large seismic networks. We then assign the template location to every subsequently detected event. To ensure the catalog contains only unique events, we apply a combination of geographic, temporal, and similarity-based filters. Events that occur within 4 s and 10 km of each other were assessed for redundancy. We perform an iterative removal events with lower inter-template correlation coefficients (<0.10) or higher location uncertainties, prioritizing the retention of the most reliable detections.

3.5 Magnitude and b-value estimation

To complete our earthquake catalog, we compute the moment magnitude using generalized parameters (see Table S1, and Hanks & Kanamori, 1979)

$$M_\mathrm{w} = \frac{2}{3}(\log_{10} M_0 - 9.1), \tag{2}$$

where M_0 is the seismic moment, derived from the stacking and fitting of the Brune model (Brune, 1970) to the S-wave displacement spectra recorded by the seismic network (Satriano, 2021). The obtained M_0 values are then integrated into Equation 2 to compute M_w. Moment magnitude is advantageous for representing earthquake size, as it does not suffer from saturation and remains reliable across a broad range of seismic events. However, estimating M_w for small earthquakes is challenging because their related ground motion is often masked by background noise. Accurate estimation of M_w for these minor events relies heavily on the sensitivity of instruments and the density of near-field stations.

Therefore, for smaller events or when data quality is insufficient, we estimate M_w from a calibration of M_L to homogenize our catalog (Deichmann, 2017). For this purpose, we estimate a local magnitude, M_L, by simulating a Wood-Anderson seismograph (Richter, 1935)

$$M_L = \log_{10} A + \log_{10} \frac{\delta}{100} + 0.00301(\delta - 100) + 3. \tag{3}$$

We use the default parameters from California as a reference (Table S2), which are enough to provide a practical comparative baseline (Equation 3). In this equation, A represents the peak-to-peak amplitude of the S wave recorded by the simulated Wood-Anderson seismometer and δ is the hypocentral distance to each station (Bakun & Joyner, 1984; Satriano, 2021).

We analyze the frequency and distribution of magnitudes across our study area, with the widely applied linear logarithmic relationship (Gutenberg & Richter, 1944)

$$\log_{10} N(\geq M) = a - bM, \tag{4}$$

where $N(\geq M)$ represents the cumulative number of earthquakes with magnitudes greater than or equal to M. The constant a estimates the seismic activity level in the region, while b indicates the relative proportion of high- to low-magnitude earthquakes, typically near 1. These parameters also serve to determine the catalog's magnitude of completeness M_c defined as the minimum magnitude at which the likelihood of detecting all earthquakes approaches 1. However, this analysis may be biased in cases of periodically low availability of stations or general incompleteness within the dataset.

To address the challenges in estimating the b-value, we applied the b-more-incomplete method (Lippiello & Petrillo, 2024), which builds upon the b-positive method (van der Elst, 2021) but improves accuracy by artificially increasing the level of incompleteness in the catalog before estimating b. While the b-positive method calculates b from positive magnitude differences between successive earthquakes, the b-more-incomplete method enhances robustness by filtering out smaller events that could introduce bias due to partial detection. This artificial filtering helps mitigate the effects of short-term aftershock incompleteness (STAI), ensuring that the estimated b-value is less affected by time-dependent variations in detection thresholds and to minimize the effects of overlapping coda waves and sparse network coverage in the catalogs, resulting in a more accurate b-value estimation.

4 Results

4.1 Earthquake catalog

We first present our machine learning-based catalog that covers 10 months of aftershock activity, recording 374,058 earthquakes from March 12, 2010, to January 24, 2011. At first, we detect 99,137 events with a minimum of five P-wave and five S-wave arrival picks. Figure 4 presents the three stages of the relocation process in two rows: the top row illustrates the entire study area, while the bottom row provides a close-up view of Pichilemu (34°S-35°S), where aftershock activity was very intense. Figure 4a-a' shows the first stage with absolute locations where the seismicity distribution appears mostly scattered. However, we can still distinguish two main types of earthquakes: a shallow component, related to a crustal component, and a deeper component, with most events located up to 50 km in depth, related to the subduction slab. In Figure 4a, we also identify that many events in the outer-rise zone (offshore, north of the rupture area, delineated by a dashed red ellipsoid) are located at depths even below 40 km.

In a second stage, we relocate the events adjusting the time residuals for each station, as shown in Figures 4b-b'. We now observe that most of the seismicity in the outer-rise zone has shifted to shallower depths, clustered seismic patches are more evident along the rupture zone and we identify clear patches with no detections, specially in the south. Finally, a total of 41,250 events (41.6 % of the initial catalog) are successfully relocated relative to nearby events, as presented in Figures 4c-c'. Here seismic patches become less diffuse and we can better distinguish geotectonic structures (e.g., Pichilemu fault system, Figures 4c').

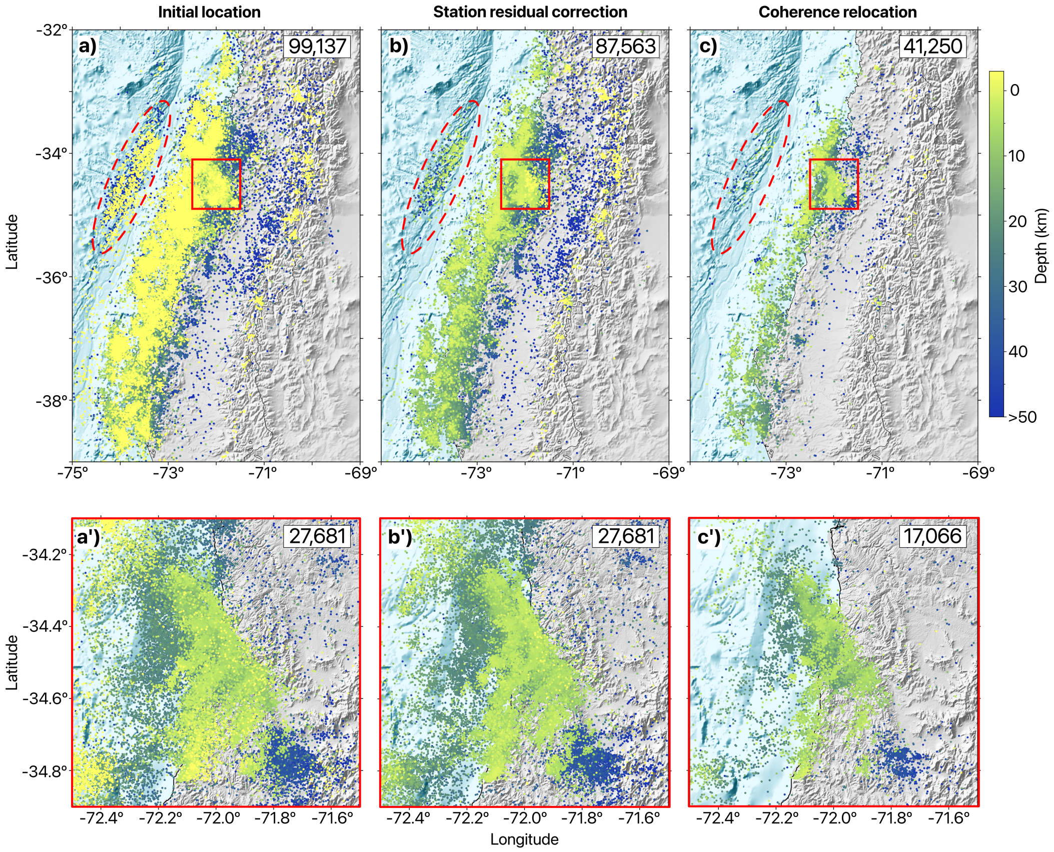

Figure 4. Earthquake locations at different steps of the relocation process. Panels **(a–c)** show the entire study area at different stages of relocation. The dashed red ellipsoid outlines the outer-rise zone, and the red box marks the area of the Pichilemu fault **(a'-c')**. **(a)** Initial locations based on automatic picks by PhaseNet. **(b)** Time residual corrections between observed picks and theoretical seismic phase arrivals, applied to the entire initial catalog. **(c)** Relative relocation based on coherence of nearby seismic signals, which could only be applied to a subset of earthquakes, primarily those near the IMAD network. **(a'–c')** Close-up view of the Pichilemu fault system, an area with a high concentration of aftershocks.

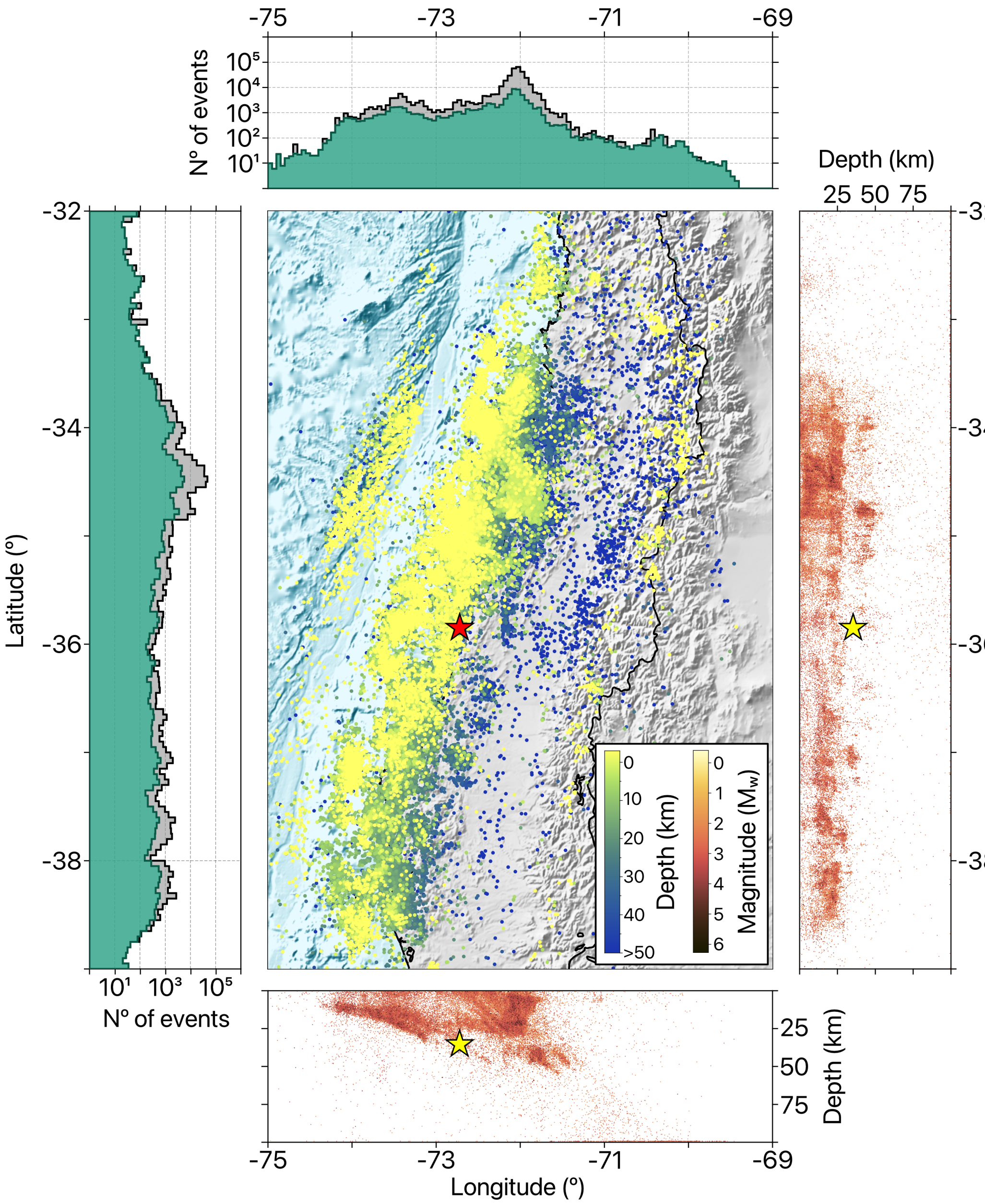

Figure 5. Spatial distribution of the aftershocks in the study area. The central panel correspond to the final locations of the whole catalog, including the coordinates of the $M_w\,8.8$ mainshock, depicted with a red star and color coded by depth. The top and left panels respectively show the number of earthquakes as a function of longitude and latitude. The green histograms represent the initial catalog, while the grey histograms represent the final catalog after template matching. The right and bottom panels display stacked depth profiles of the earthquake catalog. The bottom panel clearly illustrates subduction across different longitudes, while the right panel shows the concentration of seismicity with latitude as a function of depth. The yellow star marks the location of the mainshock.

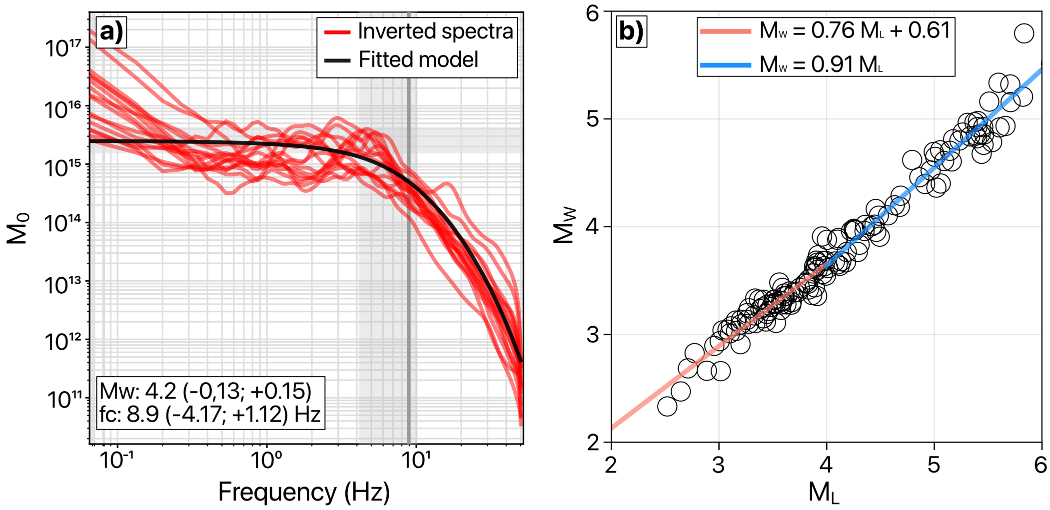

Figure 6. Magnitude estimation method for the earthquake catalog. (a) Seismic moment M_0 plotted against the frequency content of the seismic signal for an example event. Red lines show the displacement spectra recorded at different stations for this event, with Brune's model fitted to the stacked spectra (black line). The vertical dark gray rectangle indicates the estimated corner frequency. **(b)** Local magnitude M_L calibration for moment magnitude $M_\mathrm{w}$estimation for nearly 30,209 earthquakes in our catalog, represented by data with low standard deviation values.

From the relocation process, we initially identify 31,444 well-located earthquakes (with location uncertainties below 10 km) to serve as templates for template matching. To prevent redundant detections caused by highly similar events, we perform a waveform cross-correlation analysis, removing duplicates and retaining a set of 8,930 unique templates. Applying template matching with these events results in the detection of 275,913 new earthquakes, increasing the number of events by a factor 30 compared to the starting subset of templates. To maintain consistency with the scope of this study, we assign the locations of these newly detected events to their corresponding parent template, assuming a closely spaced source for each event. As shown in the histograms in Figure 5 (top and left panels), the green area represents the initial catalog, while the gray area corresponds to the final catalog after template matching, with bin sizes of 0.1°. Most seismicity is concentrated in the Pichilemu area (34–35°S, 71.5–72.5°W), where we identify the highest density of events both before and after template matching.

To ensure a consistent magnitude scale across our catalog, we use a two-step approach. First, we compute a local magnitude M_L (Equation 3) for all the events. Then, we estimate the moment magnitude M_w for a subset of 145 well-recorded reference events, selected for their low M_w uncertainties and their strong correlation with M_w values reported in other catalogs (e.g., the International Seismological Center, Di Giacomo et al., 2018). These events serve as a calibration subset to develop an empirical relationship between M_L and M_w. Figure 6a illustrates the stacking process of the displacement spectra from multiple stations for an earthquake (see also Figure S6 in Supporting Information), used to estimate the seismic moment M_0 and derive M_w (Equation 2). Based on this information, we calibrate the local magnitude M_L to estimate M_w for the entire catalog using the following relationship:

$$M_\mathrm{w} = \begin{cases} 0.76M_L + 0.61 & \text{if } M_L \leq 4, \\ 0.91M_L & \text{otherwise.} \end{cases} \tag{5}$$

These two equations reflects the empirical observation that the scaling between M_L and M_w deviates from linearity at low magnitudes. Following the approach presented by Deichmann

(2017), small earthquakes tend to follow a steeper scaling (approximately 1,5:1), while moderate-to-large events approach a 1:1 relationship. We applied a maximum likelihood bilinear regression and identified a break point at $M_L = 4$. This transition is consistent with previous studies (e.g., Deichmann, 2017), but the precise break point may vary depending on the dataset.

This approach homogenizes the catalog magnitude types, delivering M_w ranging from -0.34 to 6.50, with an average 1.86 and a completeness magnitude M_c of 1.7. The majority of events cluster at lower magnitudes, with the first quartile at M_w 1.49, the median at M_w 1.74, and the third quartile at M_w 2.12. Approximately 90 % of the events have magnitudes below M_w 2.59. Periodic spikes in event counts indicate intervals of increased seismicity, likely corresponding to aftershock sequences. Most events fall within the M_w 2–3 range, while larger magnitudes, up to M_w 6, are concentrated in the Pichilemu region, which also recorded the two largest aftershocks (M_w 7 and 6.9). However, the seismic network became fully operational only a few days after these two events, so they are not included in this catalog.

4.2 Frequency-magnitude distribution and *b*-value

The temporal variation in the number of available IMAD stations since March 12, 2010, is shown in Figure 7a, along with the location uncertainties of earthquakes. Station availability fluctuates significantly, specially after the first three months, where a steady decline is observed, aside from short week-long fluctuations. Toward the end of the period, station availability stabilizes at approximately 15 stations. These fluctuations directly affect earthquake detection and location accuracy, with periods of reduced station coverage corresponding to increased location uncertainties (Figure 7a). This effect is also evident in Figure 7b, where regions with a dense station coverage (Figure 1b), such as Pichilemu (34–35°S), exhibit a higher density of events. Conversely, regions with lower station availability exhibit detection gaps, particularly between 35 S and 37 S after 100 days from the start of the study. The larger-magnitude events are predominantly concentrated in the beginning of the sequence and mostly related to the Pichilemu area. As shown in Figure 7c, the magnitude distribution over time highlights a concentration of magnitudes around M_w 2. Looking a the earthquake detection rates (Figure 7c), we observe the expected decay over time, with occasional swarms that correspond to station reactivation. This emphasizes the large impact of station availability in the interpretation of earthquake catalogs.

We compute the *b*-value using two different methods, as illustrated in Figure 7d. For this analysis, we use batches of 6,000 earthquakes to estimate the *b*-value over time. The black line represents the *b*-values obtained using the classical maximum likelihood method for events above M_c, while the red line corresponds to estimates from the *b*-more-incomplete method (Lippiello & Petrillo, 2024). Notably, at the beginning of the sequence, *b*-values fluctuate between 1 and 1.3 until station availability begins to decline over time. As more stations become unavailable, we observe a progressive decrease in the *b*-value, reaching approximately 0.8.

5 Discussion

5.1 Geotectonic implications

This catalog provides a unprecedented high-quality view of the aftershock sequence of the 2010 Maule earthquake, particularly in the Pichilemu area, where the post-seismic activity was most intense (Figure 8, B-B'). The normal-faulting nature of this system and its potential reactivation within the area of highest coseismic slip have been documented (Farías et al., 2011; Lange et al., 2012; Ryder et al., 2012; Lieser et al., 2014). Yet, we provide a more detailed analysis of the seismotectonic structure related to the Pichilemu fault system, as illustrated in Figure 9. Seismicity related to this fault system was isolated

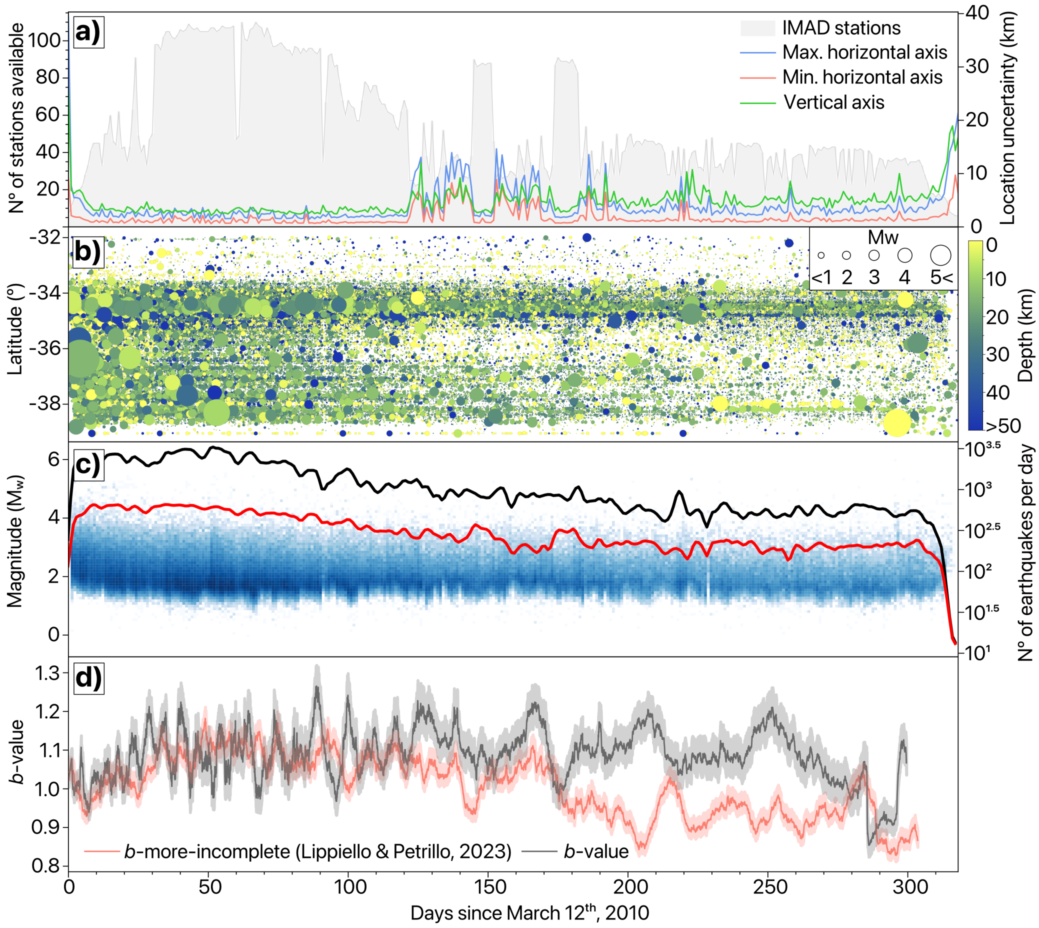

Figure 7. Temporal variations in **(a)** station availability (gray area) and earthquake location uncertainties (colored lines for maximum axis, minimum axis, and depth), **(b)** the spatial distribution in latitude, where circle size represents event magnitude and color indicates depth, **(c)** the magnitude variation in the final catalog (blue squares), and the trends accounting for the number of earthquake detected per day, from the initial catalog (red) and the final catalog (black), and **(d)** the estimated *b*-value using the *b*-more-incomplete method. Shaded areas indicate the uncertainty ranges for both methods.

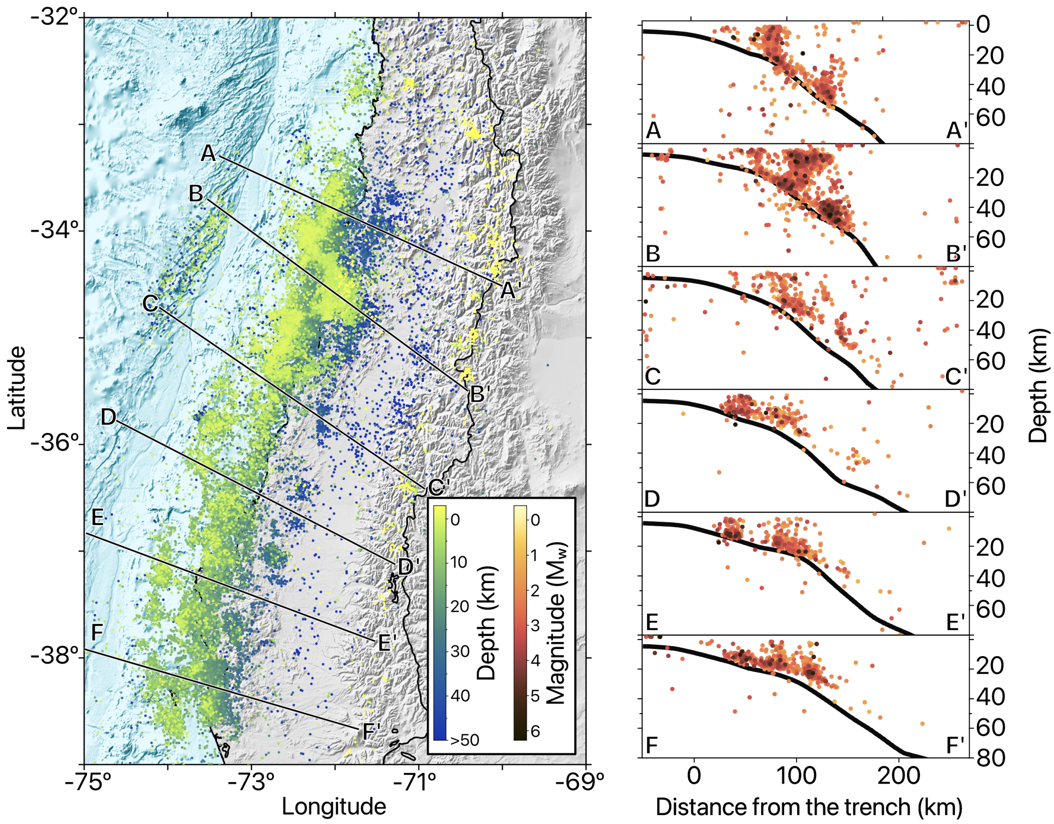

Figure 8. Spatial distribution of seismicity (colored dots) and profiles perpendicular to the subduction trench (black lines, A-F). On the left panel, color represents depth, while in the cross-sections on the right (A-F), color indicates magnitude. Black lines in the cross-sections correspond to the slab model (Slab 2.0, Hayes, 2018) for the subduction zone in this region.

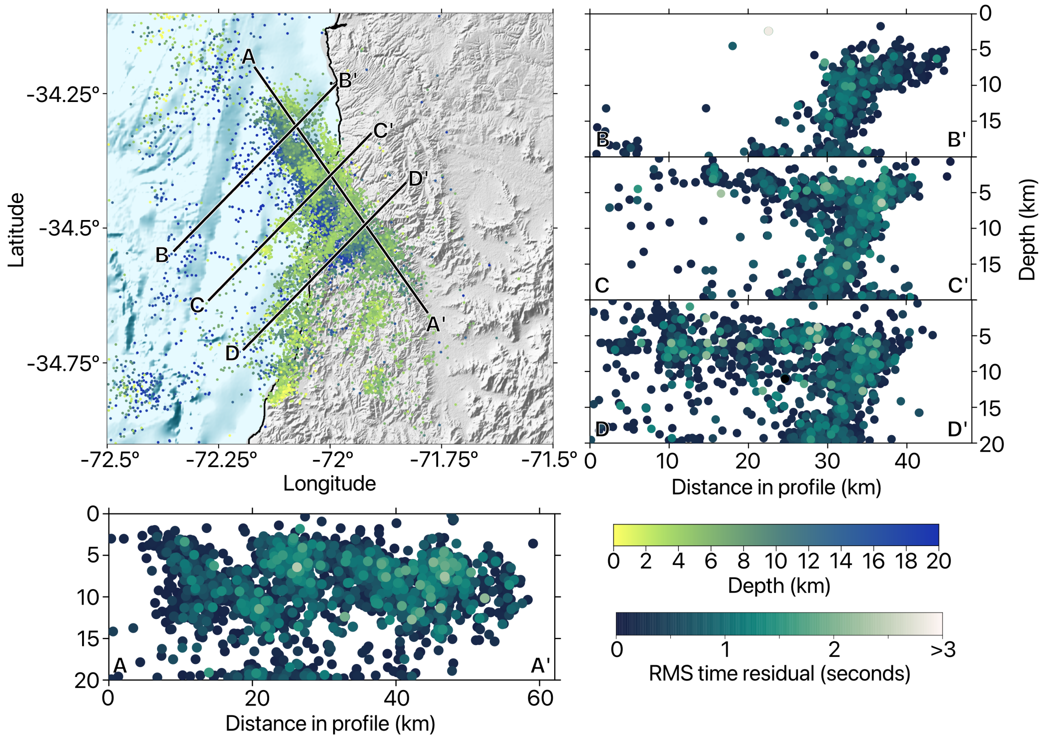

Figure 9. Spatiotemporal evolution of the Pichilemu fault system. Earthquakes are shown as dots color-coded by depth in the latitude-longitude map, and by the time residuals RMS in the cross-sections. Profiles along the black lines (A-D) include one in the main Pichilemu fault's azimuthal direction (A-A') and three perpendicular sections (B-D). The cross-sections illustrate the southwest dip direction of the northwest-trending fault and a series of conjugate faults, forming an L-shaped faulting system.

using HDBSCAN, a hierarchical density-based algorithm (Campello et al., 2013), often used as solution to distinguish earthquake patterns within catalogs (Essing & Poli, 2024). The clustering was applied in four dimensions considering location coordinates and time. We observe a main fault characterized by an azimuth-dip orientation of N40°W/S30°W and extends approximately 49 km (Figure 9, A–A'). Interestingly, the fault system exhibits distinct seismic patterns, with branches perpendicular to the main fault, forming an L-shaped distribution. This geometry suggests a complex conjugate fault system, which likely developed in response to crustal stress accommodation, similar to other documented cases of seismic sequences such as the M 6.5 Ludian earthquake (Li et al., 2024) and the M_w7.1 Ridgecrest earthquake (Liu et al., 2019). The primary NW–SE striking fault dips at about 30°SW, while secondary NE–SW branches intersect it. Seismicity is concentrated between 5 and 20 km depth along these intersecting faults, reflecting a complex fault network consistent with stress redistribution following major earthquakes.

Offshore Pichilemu, we also observe an increased seismic activity in the outer-rise zone. This finding aligns with previous studies, which suggest that this seismicity is a direct response to the high co-seismic slip in the region, potentially resulting from the activation of shallow normal fault systems under extensional forces following large slip events (Moscoso & Contreras-Reyes, 2012; Lange et al., 2012; Rietbrock et al., 2012; J. A. Ruiz & Contreras-Reyes, 2015). However, earlier studies have located these events at depths exceeding 30 km, where brittle rupture is generally unexpected (Lange et al., 2012; Rietbrock et al., 2012). In

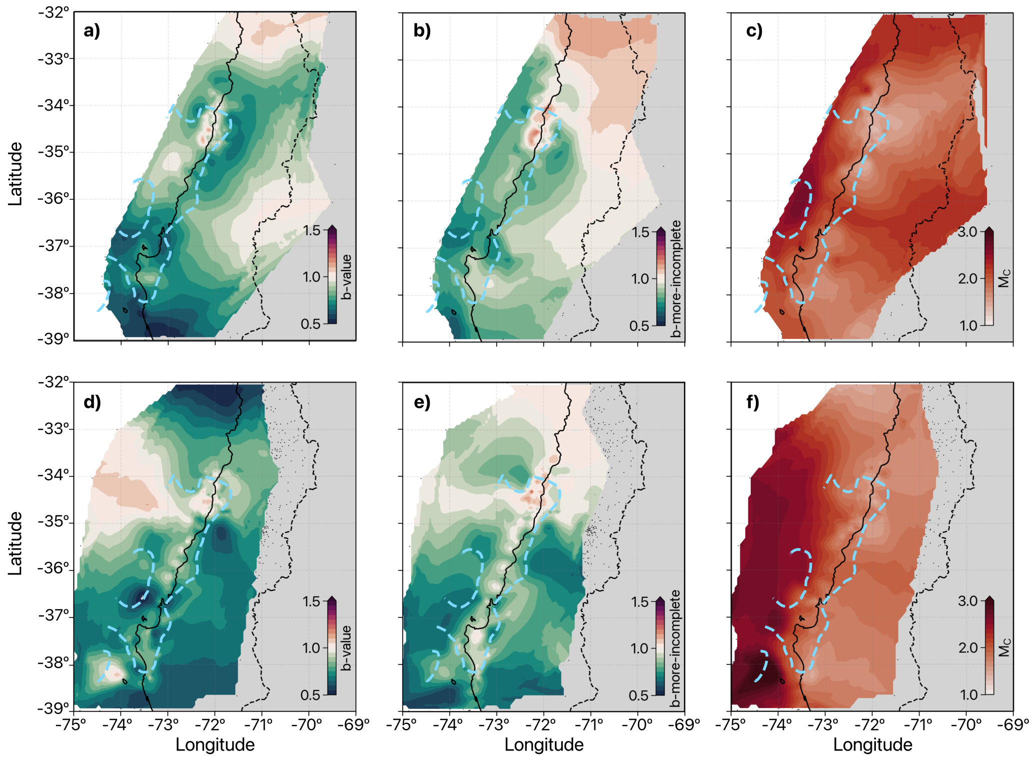

Figure 10. Spatial distribution of the *b*-value and M_c. We compute these values within earthquakes clusters of at least 100 earthquakes, for **(a–c)** shallower events associated with crustal seismicity, and **(d–f)** deeper slab-related and intraplate events. We estimate the classical *b*-value in (a) and (d), the *b*-more-incomplete in (b) and (e), and the M_c estimates in (c) and (f). The dashed blue line corresponds to the slip model (Yue et al., 2014) interpolated at 5 m.

contrast, our results improve the location accuracy of most of these events, showing a higher concentration at depths shallower than 20 km, as illustrated in Figure 8, sections B and C. Nonetheless, some depth-related artifacts persist, particularly for events below 40 km, where uncertainties remain high. These discrepancies may also stem from errors in phase-picking due to the considerable distance between the seismic sources and the network.

Intra-slab seismic activity associated with the subduction interface is present throughout the rupture zone. Notably, two distinct bands of seismicity are observed along the profiles: one at depths of 20 km to 35 km (Figure 8, A–F) and another, deeper band at approximately 50 km, primarily in Figure 8, A–C. Interestingly, a horizontal gap in seismicity is evident in the region closest to the mainshock (Figure 5), suggesting minimal post-mainshock activity in this area, likely due to significant coseismic stress release. While some seismicity does not align precisely with the slab model, it follows a consistent depth distribution, highlighting distinct tectonic behaviors captured by this catalog. This underscores the need for further refinement of the slab contours by incorporating better-constrained event locations.

The temporal evolution of the *b*-value provides key insights into stress redistribution dynamics (Rivière et al., 2018). Here we compare two *b*-value estimation methods, the traditional maximum likelihood (Aki, 1965) and the *b*-more-incomplete (Lippiello & Petrillo, 2024) as illustrated in Figure 7d. During the first 170 days of the study period, both methods produce similar *b*-values, fluctuating between 0.9 and 1.3. However, few weeks after, the *b*-more-incomplete shows a gradual decrease, reaching values between 0.8-1.0, while the classical method remains relatively stable between 1.0 and 1.2. Because the b-more-incomplete method corrects for catalog incompleteness and compensates for station loss over time, this decreasing trend likely reflects a real change in seismic activity rather than an instrumental artifact. However, while template matching significantly improves small-earthquake detection, its application was not uniformly distributed throughout the study region, leading to heterogeneous detection rates. In regions with higher template density, b-values are likely more reliable, whereas lower template density regions remain low reliable. By day 280, both methods converge to values around 0.8, just before a $M_{\mathrm{w}}6.2$ earthquake. A decreasing b-value is commonly associated with increasing differential stress in the crust, potentially indicating conditions favorable for larger events (Scholz, 2015; Schorlemmer et al., 2005).

To analyze the spatial distribution of the b-value, we divide the catalog into two subsets: shallow seismicity associated with crustal activity occurring at least 10 km above the slab interface, and slab-related seismicity that includes events within the Nazca plate and intra-slab processes (Potin et al., 2024). To identify spatial patterns (Herrmann et al., 2022), we segment the catalog based on the longitude and latitude of events with a mini-batch k-means clustering strategy (Hartigan, 1975; Sculley, 2010), randomly selecting the number of clusters k between 200 and 1000. We disregard clusters with fewer than 200 events to ensure statistical robustness. We chose this approach for computational efficiency and ability to produce clusters with balanced variance. We estimate the magnitude of completeness withing each cluster, along with the classical b-value, and the b-more-incomplete, and assign it to every earthquake of a given cluster. To account for variability, this process is repeated over $N = 100$ iterations, averaging the b-values and M_c obtained for each earthquake at each iteration. Finally, we interpolate the results onto a regular grid using a randomly sampled subset of the catalog, averaging over multiple iterations to obtain a spatially smoothed representation of these parameters. This strategy proves to induce stable result over the set of parameters (number of iterations, size of the cluster, disregarded clusters) as shown by the convergence study in the supplementary materials.

Figure 10 presents the spatial distribution of the b-value, b-more-incomplete, and M_c for both crustal seismicity (Figure 10a-c) and slab-related seismicity (Figure 10d-f). The interpretation of the b-value requires caution, as it may be influenced by factors such as network coverage and noise levels. For instance, an increase in the b-value alongside a higher M_c likely indicates reduced detection capabilities, where only larger earthquakes are recorded (e.g., Geffers et al., 2022). The b-more-incomplete method mitigates this bias by removing lower-magnitude events occurring within 120 seconds of a preceding earthquake, unless the later event has a higher magnitude. Counterintuitively, enforcing an incomplete catalog in such cases leads to a more stable distribution, effectively reducing detection bias and improving the reliability of b-value estimates. Furthermore, these trends align with the temporal evolution shown in Figure 7d.

A pronounced discrepancy between both methods is particularly evident in the southern segment (∼36°S–38°S), where Tassara et al. (2016) described a mechanically dry, highly coupled slab interface, where lower b-values are expected. The combination of lower b-more-incomplete values and high M_c suggests that classical b-value estimates are artificially inflated due to detection limitations rather than reflecting actual seismicity patterns. Conversely, in the northern segment (∼33°S–35°S), where fluid-rich subduction weakens the interface (Tassara et al., 2016; Arroyo-Solórzano & Linkimer, 2021), both methods consistently yield higher b-values, supporting the expected tectonic behavior. Additionally, regions with the highest co-seismic slip exhibit b-values consistently above 1 in both methods. In Figure 10, the blue dashed line represents the 5-meter slip contour from the coseismic slip model (Yue et al., 2014). Notably, b-value reductions are concentrated around these zones, suggesting a potential correlation between high stress release (higher b-values) and stress accumulation (lower b-values) in adjacent areas. This pattern may provide further evidence of stress redistribution following major seismic events.

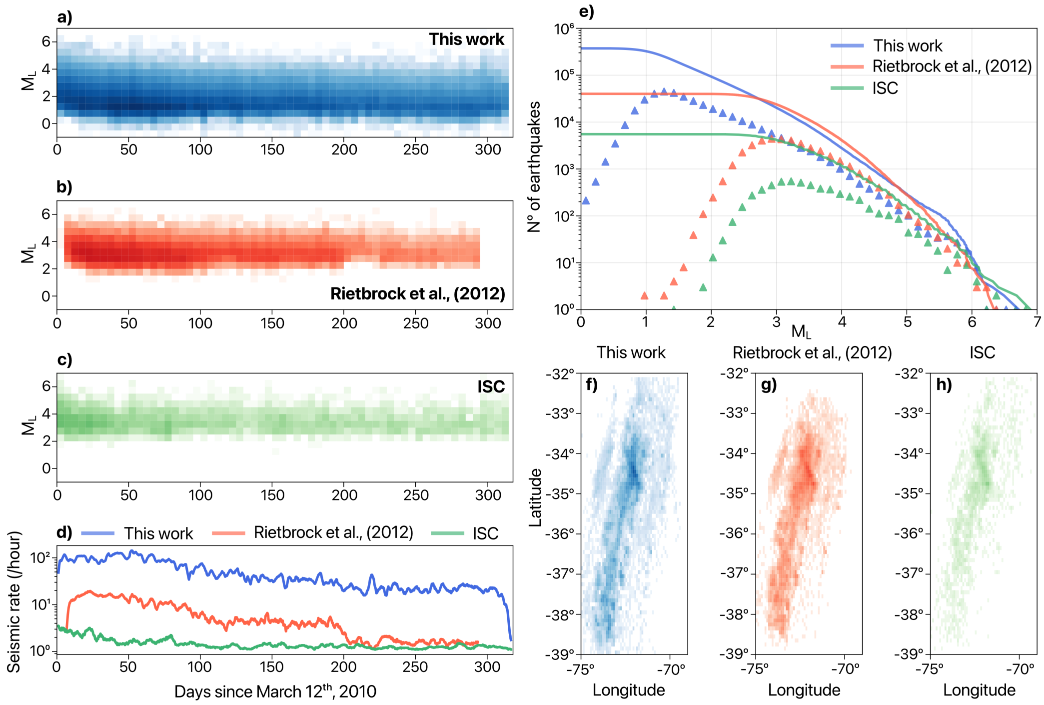

Figure 11. Comparison of earthquake catalogs based on magnitude distribution, temporal evolution, and spatial coverage. **(a)**, **(b)**, and **(c)**: 2D histograms showing the distribution of local magnitudes (M_L) over time with bins of 5 days and 0.5 in magnitude. Blue represents the catalog presented in this study, red corresponds to the catalog by Rietbrock et al. (2012), and green denotes the catalog from the ISC. Lighter tones indicate lower data density, while darker tones represent higher densities. **(d)**: Seismicity rate (events per hour) over time for the three catalogs, following the same color coding. **(e)**: Magnitude-frequency distribution for the three catalogs. Solid lines represent the cumulative number of events following the Gutenberg-Richter law, while triangles indicate the number of earthquakes for each magnitude bin. **(f)**, **(g)**, and **(h)**: Spatial distribution of seismicity in the rupture zone for each catalog.

5.2 Comparison with previous catalogs

This aftershock sequence has already been the focus of previous studies, resulting in the development of earthquake catalogs. For instance, Lange et al. (2012) utilized automatic picking methods to compile a catalog of over 20,000 events spanning the first six months of the sequence. Similarly, Rietbrock et al. (2012) applied the STA/LTA triggering method with 2D velocity models, detecting and locating approximately 30,000 earthquakes. Additionally, Ryder et al. (2012) produced a catalog using comparable methods, although limited to a shorter period of two and a half months. These catalogs have served as the basis for numerous subsequent studies, including the characterization of afterslip seismic patterns (Agurto et al., 2012) and the development of velocity models through local earthquake tomography, which have revealed new structural features in this segment of the subduction zone (Hicks et al., 2014). Major structures associated with the Maule earthquake rupture, such as those linked to the subduction slab and the crustal portion with high seismic activity near Pichilemu, are well-represented in these catalogs (e.g., Ryder et al., 2012) and are consistent in the seismicity distribution. However, the resolution of fine-scale seismic structures has remained limited.

Our study employs advanced detection and relocation techniques, particularly deep-learning-based seismic phase picking, to enhance the completeness and accuracy of the earthquake catalog. A key advantage is the improved resolution of fine-scale fault structures, enabled by detecting a significantly larger number of small-magnitude earthquakes. This improvement is primarily attributed to PhaseNet, which identified at least three times more seismic phases within the same dataset compared to conventional methods such as STA/LTA and SNR, as demonstrated in previous studies. The increased resolution provides deeper insights into the spatial distribution and connectivity of fault structures within the rupture zone, corroborating previous findings while uncovering additional structural details. For further details on relocation accuracy, refer to Text S1 and Figure S7. We successfully re-detect approximately 88 % of the events reported by Rietbrock et al. (2012) and 90 % of those cataloged by the Centro Nacional de Sismología de Chile (CSN) and the International Seismic Catalog (ISC) (Di Giacomo et al., 2018). The remaining events are likely excluded due to insufficient seismic picks in our dataset, limiting the processing of these signals. While these signals may correspond to real seismic events, they fail to meet the stringent criteria required for consistent processing within our methodology. By excluding them, we ensure the robustness, homogeneity, and reliability of our catalog.

Figure 11 compares the magnitude distribution, temporal evolution, and spatial coverage of seismicity in three catalogs: Rietbrock et al. (2012), the ISC catalog (Di Giacomo et al., 2018), and ours. While all catalogs achieve consistent detection completeness for $M_L \geq 3$, our catalog captures a significantly higher number of small-magnitude events ($M_L \leq 2$). This improvement is especially evident during periods of low station coverage, where our catalog maintains consistency, while detection capabilities decline in the other datasets. The seismicity rate, as shown in Figure 11d, highlights similar temporal trends across the three catalogs, with notable differences in the total number of events recorded. A significant observation is the local reduction in the detection capacity after larger earthquakes, which leads to noticeable drops in the seismicity rate. This phenomenon reflects the saturation of seismic signals by the coda waves of larger events, which hinders the detection of smaller aftershocks. These biases, evident in all three catalogs, occur consistently at the same moments in the temporal distribution of seismicity. This highlights the importance of accounting for detection limitations when interpreting seismic activity, as they can significantly affect the analysis of aftershock sequences and trends.

The frequency-magnitude distribution of our catalog, compared to the catalogs of Rietbrock et al. (2012) and the ISC, is presented in Figure 11e. This comparison highlights the improved detection capability of the proposed workflow, which achieves a lower magnitude of completeness by 1 to 2 orders of magnitude, significantly expanding the range of detectable seismic events. Nevertheless, some differences in the number of moderate-to-large magnitude events are also observed across the three catalogs. These discrepancies are mainly related to the way local magnitudes are computed, as each catalog relies on a different magnitude scaling (see our case: Equation 3). In addition, the period covered is shorter in the case of the catalog from Rietbrock et al. (2012), which likely misses some events. For the ISC catalog (e.g., Di Giacomo et al., 2018), the lack of a local network further limits the number of detected earthquakes, particularly in the lower and intermediate magnitude ranges. Figure 11f–h show the overall shape of the seismicity distribution is consistent between catalogs, with a pronounced concentration around the Pichilemu region. However, our catalog reveals previously undetected zones of seismic activity, demonstrating the enhanced detection and location accuracy achieved with our workflow.

5.3 Workflow performance and limitations

In this study, we implement an automated detection-location workflow (Beaucé et al., 2024) and present a new catalog covering up to ten months of the Maule earthquake aftershock sequence. Our results demonstrate that, despite certain limitations in dataset quality, modern algorithms can significantly improve the completeness and precision of earthquake catalogs. However, the accuracy of these methods remains strongly dependent on the spatiotemporal coverage of the seismic network, underscoring the persistent challenges associated with station density and distribution. For detection and location, we employed the automated seismic phase-picking model PhaseNet, a widely recognized tool for its effectiveness in phase detection (Tan et al., 2021; Chen et al., 2022; Feng et al., 2022; Jiang et al., 2022; Duan et al., 2023; Gong et al., 2023). This algorithm significantly enhanced detection capabilities while greatly reducing the time required for manual phase picking. In this study, we used the pre-trained *PhaseNet* model from northern California, which has demonstrated robust performance across diverse geotectonic contexts (Retailleau et al., 2022). However, its precision is still sensitive to high noise levels, particularly in regions with high anthropogenic sources, and its performance decreases for distant earthquakes where the P-S arrival time difference exceeds 30 s.

In addition, we used beamforming (Frank & Shapiro, 2014; Beaucé et al., 2019, 2022, 2024) to obtain the source location likelihood of the initial catalog. However, this approach is highly sensitive to the chosen detection threshold in the daily composite network response (Figure 3). While previous studies have validated the use of fixed thresholds (e.g., Beaucé et al., 2024), our findings reveal the advantages of implementing a variable threshold for incomplete datasets. Specifically, we propose a criterion based on the 97^{th} percentile of the daily cumulative density function, which dynamically adjusts to variations in data quality caused by fluctuations in station and channel availability. This threshold was optimized through performance testing to balance computational efficiency and detection accuracy, selecting the value that provided the best detection ratio. However, we acknowledge that this approach inherently imposes a detection rate, meaning that on days with low seismic activity, it may lead to an increased number of false detections. Despite this limitation, the adaptive thresholding method significantly improves the reliability of seismic records by reducing the likelihood of missed detections during periods of higher seismic activity.

The quality of seismic phase picking remains a critical factor in determining the accuracy of earthquake locations, with certain limitations persisting, particularly for distant events. Offshore events in the outer-rise zone, for example, present specific challenges due to the predominantly north-south orientation of the seismic array, which restricts azimuthal coverage and affects location precision. Nevertheless, the relocated hypocenters show a clear NNE alignment, consistent with the expected rupture geometry. Additionally, the accuracy of the velocity model plays a pivotal role in refining earthquake locations, emphasizing the need for further improvements in model precision. While a 1D velocity model is enough for many detection-location routines, it is inadequate for large regions like our study area, which is characterized by significant geological heterogeneities. In such cases, 3D tomography velocity models are highly beneficial as they capture velocity variations across latitude, longitude, and depth. However, while 3D models can provide valuable large-scale details, their accuracy may still be limited in specific local contexts. For instance, in our case, a 1D model fails to adequately represent the velocity structure, yet even a 3D model (Potin et al., 2024) can be oversimplified in certain zones, for example, in the outer-rise zone, the velocity model remains poorly constrained due to limited seismic data. Similarly, in the southern part of the rupture zone, the scarcity of seismic events hinders the accuracy of a robust model. Therefore, an adapted approach was still required, as proposed for the scope of this work introducing the slab geometry. Nonetheless, the results presented in Potin et al. (2024) demonstrate notable outcomes at greater scales, and the velocity model employed provides a valuable base for refining the Maule region's tomography for future relocation processes.

To assign local magnitudes (M_L), we implemented a standard empirical relation (Equation 3) originally developed for Californian tectonic conditions, which relates the maximum S-wave amplitude and hypocentral distance. Although this relationship was not calibrated specifically for the Maule region, it provides a consistent and computationally efficient method for magnitude estimation across thousands of detections. To evaluate the adequacy of this model in our context, we performed a residual analysis comparing the observed amplitudes against those predicted from the calculated M_L values. The results (Figure S8 in Supplementary Information) show a systematic negative residual with an average offset of approximately one logarithmic unit in amplitude. This implies that the model tends to overpredict the amplitudes observed in this region, likely due to regional differences in attenuation not captured by the original formulation. Interestingly, this offset remains roughly constant across the range of distances and magnitudes, although a slight distance-dependent trend is present, with more negative residuals at close distances and occasional positive residuals beyond 40 km. Despite this systematic bias, the use of Equation 3 remains justified and the relationship provides relative consistency across the dataset, and the observed offset does not significantly distort relative magnitude comparisons or downstream statistical analyses such as b-value estimation. We explicitly acknowledge this limitation and show that the deviation is primarily a uniform offset rather than a structural mismatch, allowing the method to remain valid within the scope of regional catalog construction and seismicity analysis. These findings highlight the importance of future work focused on separating the physical components of ground motion, including source, path, and site effects. Better understanding these parameters can improve magnitude estimation models and support more reliable seismic hazard assessments.

6 Conclusion

This study presents a catalog of the aftershock sequence of the 2010 $M_\mathrm{w}8.8$ Maule earthquake in Chile from March 2010 to March 2011. We obtain the catalog from a reanalysis of the past data with BPMF, an advanced detection-location workflow that relies on PhaseNet-based phase picking, a high-precision relocation algorithms (NonLinLoc-SSST-Coherence), and template matching to construct a high-resolution earthquake catalog. This workflow enables the identification of over 375,000 earthquakes, which is 12 times more than existing catalogs (Rietbrock et al., 2012). The catalog includes detailed uncertainties in both location and magnitude, offering an unprecedented level of detail for understanding post-seismic activity within the rupture zone.

One of the significant challenges addressed in this study is the varying availability of the seismic network over time, and the overall temporal coverage of the experiment. The IMAD mobile seismic network, deployed weeks after the mainshock, provided sparse data, generating obstacles for accurate and consistent detection and location of seismic events. By optimizing detection capabilities, we overcome these limitations to deliver a precise and comprehensive catalog. This approach also helps to refine and uncover fine-scale seismic structures with greater detail, consolidating patterns that were previously scattered, particularly in regions of heightened activity, such as the northern rupture area near Pichilemu. Additionally, this catalog spans a wide range of magnitudes (M_w -0.34 to 6.50), encompassing seismic events distributed across the subduction slab and shallow crustal regions. It achieves a magnitude of completeness of about $M_\mathrm{w}1.7$, reducing it by an order of magnitude compared to previous catalogs.

Spatial b-value variations across the rupture zone suggest structural segmentation and localized differences in stress conditions. Elevated b-values near Pichilemu are associated with a predominance of small-magnitude earthquakes, which may reflect low differential stress and elevated pore fluid pressure. This condition could reduce effective normal stress, promoting fault weakening and facilitating the reactivation of upper-plate structures. In contrast, lower b-values to the south may indicate higher differential stress and stronger mechanical coupling, typical of locked asperities that accumulate strain and rupture in larger events. These spatial patterns support the idea that fluid distribution and inherited structure play a key role in shaping frictional strength and rupture behavior along the megathrust. Further constraints from stress drop, corner frequency, and afterslip models may help refine this interpretation. Additionally, the improved location accuracy allows a clearer delineation of zones with little or no seismic activity, which may indicate aseismic patches now better constrained spatially. These areas could be more effectively characterized in future studies.

This study highlights the broader potential of automated workflows to advance earthquake monitoring and analysis. The methodology's precision and adaptability ensure its applicability to other earthquake sequences and diverse geotectonic contexts. Future research can build on this work by integrating advanced velocity models to improve relocation accuracy and by incorporating additional tomography. These developments could refine our understanding of the physical mechanisms driving seismicity and provide critical insights into subduction zone dynamics, the interplay between rupture dynamics, stress redistribution, and post-seismic deformation processes. Moreover, the results have practical implications for seismic hazard evaluation, offering tools to address challenges in mitigating risks associated with large subduction earthquakes.

Data Availability Statement

The seismic data used in this study is publicly available through the RESIF (`https://seismology.resif.fr`), IRIS (`https://www.iris.edu/hq/`), and GEOFON (`https://geofon.gfz.de/`) data servers. It was collected as part of the temporary mobile network deployed during the 2010 Maule aftershock sequence, with seismic instruments provided by CNRS-INSU, IRIS/PASSCAL, GIPP (GFZ), and GEF/SeisUK. Supplementary materials, including workflow details, are provided in Supplementary Figure S1, while the complete earthquake catalog is available in Supplementary File S2. The algorithms used in this study are also open and accessible: the BackProjection and Matched Filter (BPMF) workflow can be found at `https://github.com/ebeauce/Seismic_BPMF`, the NonLinLoc-SSST-Coherence algorithm at `http://alomax.free.fr/nlloc/`, and SourceSpec at `https://github.com/SeismicSource/sourcespec`. Additionally, the implementation of various b-value estimation methods is available at `https://github.com/caccioppoli/b-more-positive`.

Acknowledgments

This work was funded through the ANR-22-CPJ1-0020-01 program. E. Beaucé was funded by the Brinson Foundation. L.F. Bonilla was funded by project ANR E-City, AAPG 2021 – CES 22. Continuous seismic data was provided thanks to the collaborative efforts of IRIS, IPGP, ENS, and GFZ. Numerical computations were conducted on the S-CAPAD/DANTE platform at IPGP, France. We sincerely thank Sergio Ruiz and Raúl Madariaga for their valuable discussions on seismicity in the Maule region. We also acknowledge Javier Ojeda, Leoncio Cabrera, and Martin Vallée for their insightful contributions to discussions on seismic parameters relevant to this study. Additionally, we extend our appreciation to Antony Lomax, Jannes Münchmeyer, and Bertrand Potin for their constructive feedback on the event relocation process. We also thank the Andes-FrenSZ collaboration research program and associated researchers for their valuable comments and contributions. Finally, we are grateful to all researchers at IPGP, Universidad de Chile, and ISTerre who provided thoughtful insights, discussions, and feedback that contributed to improving this study. We are very thankful to the journal editor Rachel Abercrombie, the associate editor and two anonymous reviewers for their constructive comments and suggestions that significantly contributed to improving the quality and clarity of this work.

References

Agurto, H., Rietbrock, A., Ryder, I., & Miller, M. (2012). Seismic-afterslip characterization of the 2010 mw 8.8 maule, chile, earthquake based on moment tensor inversion. *Geophysical Research Letters*, *39*(20).

Aki, K. (1965). Maximum likelihood estimate of b in the formula log n= a-bm and its confidence limits. *Bull. Earthquake Res. Inst., Tokyo Univ.*, *43*, 237–239.

Allen, R. (1982). Automatic phase pickers: Their present use and future prospects. *Bulletin of the Seismological Society of America*, *72*(6B), S225–S242.

Anstey, N. A. (1964). Correlation techniques–a review. *Geophysical Prospecting*, *12*(4), 355–382.

Aron, F., Cembrano, J., Astudillo, F., Allmendinger, R. W., & Arancibia, G. (2015). Constructing forearc architecture over megathrust seismic cycles: Geological snapshots from the maule earthquake region, chile. *Bulletin*, *127*(3-4), 464–479.

Arroyo-Solórzano, M., & Linkimer, L. (2021). Spatial variability of the b-value and seismic potential in costa rica. *Tectonophysics*, *814*, 228951.

Bakun, W. H., & Joyner, W. B. (1984). The ml scale in central california. *Bulletin of the Seismological Society of America*, *74*(5), 1827–1843.

Båth, M. (1965). Lateral inhomogeneities of the upper mantle. *Tectonophysics*, *2*(6), 483–514.

Beaucé, E., Frank, W. B., Paul, A., Campillo, M., & van Der Hilst, R. D. (2019). Systematic detection of clustered seismicity beneath the southwestern alps. *Journal of Geophysical Research: Solid Earth*, *124*(11), 11531–11548.

Beaucé, E., Frank, W. B., & Romanenko, A. (2018). Fast matched filter (fmf): An efficient seismic matched-filter search for both cpu and gpu architectures. *Seismological Research Letters*, *89*(1), 165–172.

Beaucé, E., Frank, W. B., Seydoux, L., Poli, P., Groebner, N., van der Hilst, R. D., & Campillo, M. (2024). Bpmf: A backprojection and matched-filtering workflow for automated earthquake detection and location. *Seismological Research Letters*, *95*(2A), 1030–1042.

Beaucé, E., van der Hilst, R. D., & Campillo, M. (2022). Microseismic constraints on the mechanical state of the north anatolian fault zone 13 years after the 1999 m7. 4 izmit earthquake. *Journal of Geophysical Research: Solid Earth*, *127*(9), e2022JB024416.

Beck, S., Rietbrock, A., Tilmann, F., Barrientos, S., Meltzer, A., Oncken, O., … Russo, R. M. (2014). Advancing subduction zone science after a big quake. *Eos, Transactions American Geophysical Union*, *95*(23), 193–194.

Bilek, S. L., & Lay, T. (2018). Subduction zone megathrust earthquakes. *Geosphere*, *14*(4), 1468–1500.

Brune, J. N. (1970). Tectonic stress and the spectra of seismic shear waves from earthquakes. *Journal of geophysical research*, *75*(26), 4997–5009.

Cabrera, L., Ruiz, S., Poli, P., Contreras-Reyes, E., Osses, A., & Mancini, R. (2021). Northern chile intermediate-depth earthquakes controlled by plate hydration. *Geophysical Journal International*, *226*(1), 78–90.

Campello, R. J., Moulavi, D., & Sander, J. (2013). Density-based clustering based on hierarchical density estimates. In *Pacific-asia conference on knowledge discovery and data mining* (pp. 160–172).

Campos, J., Hatzfeld, D., Madariaga, R., López, G., Kausel, E., Zollo, A., … Lyon-Caen, H. (2002). A seismological study of the 1835 seismic gap in south-central chile. *Physics of the Earth and Planetary Interiors*, *132*(1-3), 177–195.

Chen, H., Yang, H., Zhu, G., Xu, M., Lin, J., & You, Q. (2022). Deep outer-rise faults in the southern mariana subduction zone indicated by a machine-learning-based high-resolution earthquake catalog. *Geophysical Research Letters*, *49*(12), e2022GL097779.

Deichmann, N. (2017). Theoretical basis for the observed break in ml/m w scaling between small and large earthquakes. *Bulletin of the Seismological Society of America*, *107*(2), 505–520.

Delouis, B., Nocquet, J.-M., & Vallée, M. (2010). Slip distribution of the february 27, 2010 mw= 8.8 maule earthquake, central chile, from static and high-rate gps, insar, and broadband teleseismic data. *Geophysical Research Letters*, *37*(17).

Di Giacomo, D., Engdahl, E. R., & Storchak, D. A. (2018). The isc-gem earthquake catalogue (1904–2014): status after the extension project. *Earth System Science Data*, *10*(4), 1877–1899.

Duan, L., Zhao, C., Du, X., & Zhou, L. (2023). Machine learning-based automatic construction of earthquake catalog for reservoir areas in multiple river basins of guizhou province, china. *Earthquake Science*, *36*(2), 132–146.

Essing, D., & Poli, P. (2024). Unraveling earthquake clusters composing the 2014 alto tiberina earthquake swarm via unsupervised learning. *Journal of Geophysical Research: Solid Earth*, *129*(1), e2022JB026237.

Farge, G., & Brodsky, E. E. (2025). The big impact of small quakes on tectonic tremor synchronization. *Science Advances*, *11*(20), eadu7173.

Farías, M., Comte, D., Roecker, S., Carrizo, D., & Pardo, M. (2011). Crustal extensional faulting triggered by the 2010 chilean earthquake: The pichilemu seismic sequence. *Tectonics*, *30*(6).

Felzer, K. R., Abercrombie, R. E., & Ekstrom, G. (2004). A common origin for aftershocks, foreshocks, and multiplets. *Bulletin of the Seismological Society of America*, *94*(1), 88–98.

Feng, T., Zhang, M., Xu, L., Wu, J., & Fang, L. (2022). Machine learning-based earthquake catalog and tomography characterize the middle-northern section of the xiaojiang fault zone. *Seismological Society of America*, *93*(5), 2484–2497.

Frank, W., & Shapiro, N. (2014). Automatic detection of low-frequency earthquakes (lfes) based on a beamformed network response. *Geophysical Journal International*, *197*(2), 1215–1223.

Geffers, G., Main, I., & Naylor, M. (2022). Biases in estimating b-values from small earthquake catalogues: how high are high b-values? *Geophysical Journal International*, *229*(3), 1840–1855.

Gibbons, S. J., & Ringdal, F. (2006). The detection of low magnitude seismic events using array-based waveform correlation. *Geophysical Journal International*, *165*(1), 149–166.

Glodny, J., Echtler, H., Collao, S., Ardiles, M., Burón, P., & Figueroa, O. (2008). Differential late paleozoic active margin evolution in south-central chile (37° s–40° s)–the lanalhue fault zone. *Journal of South American Earth Sciences*, *26*(4), 397–411.

Gong, J., Fan, W., & Parnell-Turner, R. (2023). Machine learning-based new earthquake catalog illuminates on-fault and off-fault seismicity patterns at the discovery transform fault, east pacific rise. *Geochemistry, Geophysics, Geosystems*, *24*(9), e2023GC011043.

Gutenberg, B., & Richter, C. F. (1944). Frequency of earthquakes in california. *Bulletin of the Seismological society of America*, *34*(4), 185–188.

Haberland, C., Rietbrock, A., Lange, D., Bataille, K., & Dahm, T. (2009). Structure of the seismogenic zone of the southcentral chilean margin revealed by local earthquake traveltime tomography. *Journal of Geophysical Research: Solid Earth*, *114*(B1).

Hanks, T. C., & Kanamori, H. (1979). A moment magnitude scale. *Journal of Geophysical Research: Solid Earth*, *84*(B5), 2348–2350.

Hartigan, J. A. (1975). *Clustering algorithms.* John Wiley & Sons, Inc.

Hayes, G. (2018). *Slab2-a comprehensive subduction zone geometry model: Us geological survey data release, doi: 10.5066.* F7PV6JNV.

Herrmann, M., Piegari, E., & Marzocchi, W. (2022). Revealing the spatiotemporal complexity of the magnitude distribution and b-value during an earthquake sequence. *Nature Communications*, *13*(1), 5087.

Hervé, F., Godoy, E., Parada, M. A., Ramos, V., Rapela, C., Mpodozis, C., & Davidson, J. (1987). A general view on the chilean-argentine andes, with emphasis on their early history. *Circum-Pacific Orogenic Belts and Evolution of the Pacific Ocean Basin*, *18*, 97–113.

Hervé, F., Munizaga, F., Parada, M., Brook, M., Pankhurst, R., Snelling, N., & Drake, R. (1988). Granitoids of the coast range of central chile: geochronology and geologic setting. *Journal of South American Earth Sciences*, *1*(2), 185–194.

Hicks, S. P., Rietbrock, A., Ryder, I. M., Lee, C.-S., & Miller, M. (2014). Anatomy of a megathrust: The 2010 m8. 8 maule, chile earthquake rupture zone imaged using

seismic tomography. *Earth and Planetary Science Letters*, *405*, 142–155.
Jiang, C., Zhang, P., White, M. C., Pickle, R., & Miller, M. S. (2022). A detailed earthquake catalog for banda arc–australian plate collision zone using machine-learning phase picker and an automated workflow. *The Seismic Record*, *2*(1), 1–10.
Lange, D., Tilmann, F., Barrientos, S. E., Contreras-Reyes, E., Methe, P., Moreno, M., ... et al. (2012). Aftershock seismicity of the 27 february 2010 mw 8.8 maule earthquake rupture zone. *Earth and Planetary Science Letters*, *317*, 413–425.
Li, J., Hao, M., & Cui, Z. (2024). A high-resolution aftershock catalog for the 2014 m s 6.5 ludian (china) earthquake using deep learning methods. *Applied Sciences*, *14*(5), 1997.
Lieser, K., Grevemeyer, I., Lange, D., Flueh, E., Tilmann, F., & Contreras-Reyes, E. (2014). Splay fault activity revealed by aftershocks of the 2010 mw 8.8 maule earthquake, central chile. *Geology*, *42*(9), 823–826.
Lippiello, E., & Petrillo, G. (2024). b-more-incomplete and b-more-positive: Insights on a robust estimator of magnitude distribution. *Journal of Geophysical Research: Solid Earth*, *129*(2), e2023JB027849.
Liu, C., Lay, T., Brodsky, E. E., Dascher-Cousineau, K., & Xiong, X. (2019). Coseismic rupture process of the large 2019 ridgecrest earthquakes from joint inversion of geodetic and seismological observations. *Geophysical Research Letters*, *46*(21), 11820–11829.
Lomax, A. (2001). *Nonlinloc home page.*
Lomax, A., Michelini, A., Curtis, A., & Meyers, R. (2009). Earthquake location, direct, global-search methods. *Encyclopedia of complexity and systems science*, *5*, 2449–2473.
Lomax, A., & Savvaidis, A. (2022). High-precision earthquake location using source-specific station terms and inter-event waveform similarity. *Journal of Geophysical Research: Solid Earth*, *127*(1), e2021JB023190.
Lorito, S., Romano, F., Atzori, S., Tong, X., Avallone, A., McCloskey, J., ... Piatanesi, A. (2011). Limited overlap between the seismic gap and coseismic slip of the great 2010 chile earthquake. *Nature Geoscience*, *4*(3), 173–177.
Madariaga, R., Métois, M., Vigny, C., & Campos, J. (2010). Central chile finally breaks. *Science*, *328*(5975), 181–182.
Mancini, S., Segou, M., Werner, M. J., Parsons, T., Beroza, G., & Chiaraluce, L. (2022). On the use of high-resolution and deep-learning seismic catalogs for short-term earthquake forecasts: Potential benefits and current limitations. *Journal of Geophysical Research: Solid Earth*, *127*(11), e2022JB025202.
Marsan, D. (2005). The role of small earthquakes in redistributing crustal elastic stress. *Geophysical Journal International*, *163*(1), 141–151.
Melnick, D., Bookhagen, B., Strecker, M. R., & Echtler, H. P. (2009). Segmentation of megathrust rupture zones from fore-arc deformation patterns over hundreds to millions of years, arauco peninsula, chile. *Journal of Geophysical Research: Solid Earth*, *114*(B1).
Minetto, R., Helmstetter, A., Schwartz, S., Langlais, M., Nomade, J., & Guéguen, P. (2022). Analysis of the spatiotemporal evolution of the maurienne swarm (french alps) based on earthquake clustering. *Earth and Space Science*, *9*(7), e2021EA002097.
Moreno, M., Rosenau, M., & Oncken, O. (2010). 2010 maule earthquake slip correlates with pre-seismic locking of andean subduction zone. *Nature*, *467*(7312), 198–202.
Moscoso, E. I., & Contreras-Reyes, E. (2012). Outer rise seismicity related to the maule, chile 2010 mega-thrust earthquake and hydration of the incoming oceanic lithosphere. *Andean Geology*, *39*(3), 564–572.
Mousavi, S. M., & Beroza, G. C. (2023). Machine learning in earthquake seismology. *Annual Review of Earth and Planetary Sciences*, *51*(1), 105–129.
Mpodozis, C., & Ramos, V. (1990). The andes of chile and argentina. *Circum Pacific Council Publications*, *11*, 59–90.
Neighbors, C., Liao, E., Cochran, E. S., Funning, G., Chung, A., Lawrence, J., ... Andrés Sepulveda, H. (2015). Investigation of the high-frequency attenuation parameter, κ (kappa), from aftershocks of the 2010 m w 8.8 maule, chile earthquake.

Geophysical Journal International, *200*(1), 200–215.

Ojeda, J., Ruiz, S., del Campo, F., & Carvajal, M. (2020). The 21 may 1960 mw 8.1 concepción earthquake: A deep megathrust foreshock that started the 1960 central-south chilean seismic sequence. *Seismological Research Letters*, *91*(3), 1617–1627.

Peng, Z., & Zhao, P. (2009). Migration of early aftershocks following the 2004 parkfield earthquake. *Nature Geoscience*, *2*(12), 877–881.

Pollitz, F. F., Brooks, B., Tong, X., Bevis, M. G., Foster, J. H., Bürgmann, R., … others (2011). Coseismic slip distribution of the february 27, 2010 mw 8.8 maule, chile earthquake. *Geophysical Research Letters*, *38*(9).

Potin, B., Ruiz, S., Aden-Antoniow, F., Madariaga, R., & Barrientos, S. (2024). A revised chilean seismic catalog from 1982 to mid-2020. *Seismological Research Letters*.

Retailleau, L., Saurel, J.-M., Laporte, M., Lavayssière, A., Ferrazzini, V., Zhu, W., … et al. (2022). Automatic detection for a comprehensive view of mayotte seismicity. *Comptes Rendus. Géoscience*, *354*(S2), 153–170.

Richter, C. F. (1935). An instrumental earthquake magnitude scale. *Bulletin of the seismological society of America*, *25*(1), 1–32.

Rietbrock, A., Ryder, I., Hayes, G., Haberland, C., Comte, D., Roecker, S., & Lyon-Caen, H. (2012). Aftershock seismicity of the 2010 maule mw= 8.8, chile, earthquake: Correlation between co-seismic slip models and aftershock distribution? *Geophysical Research Letters*, *39*(8).

Rivière, J., Lv, Z., Johnson, P., & Marone, C. (2018). Evolution of b-value during the seismic cycle: Insights from laboratory experiments on simulated faults. *Earth and Planetary Science Letters*, *482*, 407–413.

Ross, Z. E., Idini, B., Jia, Z., Stephenson, O. L., Zhong, M., Wang, X., … et al. (2019). Hierarchical interlocked orthogonal faulting in the 2019 ridgecrest earthquake sequence. *Science*, *366*(6463), 346–351.

Ruegg, J., Rudloff, A., Vigny, C., Madariaga, R., De Chabalier, J., Campos, J., … Dimitrov, D. (2009). Interseismic strain accumulation measured by gps in the seismic gap between constitución and concepción in chile. *Physics of the Earth and Planetary Interiors*, *175*(1-2), 78–85.

Ruiz, J. A., & Contreras-Reyes, E. (2015). Outer rise seismicity boosted by the maule 2010 mw 8.8 megathrust earthquake. *Tectonophysics*, *653*, 127–139.

Ruiz, J. A., Hayes, G. P., Carrizo, D., Kanamori, H., Socquet, A., & Comte, D. (2014). Seismological analyses of the 2010 march 11, pichilemu, chile m w 7.0 and m w 6.9 coastal intraplate earthquakes. *Geophysical Journal International*, *197*(1), 414–434.

Ruiz, S., Aden-Antoniow, F., Baez, J. C., Otarola, C., Potin, B., del Campo, F., … Bernard, P. (2017). Nucleation phase and dynamic inversion of the mw 6.9 valparaíso 2017 earthquake in central chile. *Geophysical Research Letters*, *44*(20), 10,290-10,297. Retrieved from `https://agupubs.onlinelibrary.wiley.com/doi/abs/10.1002/2017GL075675` doi: https://doi.org/10.1002/2017GL075675

Ruiz, S., & Madariaga, R. (2018). Historical and recent large megathrust earthquakes in chile. *Tectonophysics*, *733*, 37–56.

Ruiz, S., Madariaga, R., Astroza, M., Saragoni, G. R., Lancieri, M., Vigny, C., & Campos, J. (2012). Short-period rupture process of the 2010 mw 8.8 maule earthquake in chile. *Earthquake Spectra*, *28*(1_suppl1), 1–18.

Ryder, I., Rietbrock, A., Kelson, K., Bürgmann, R., Floyd, M., Socquet, A., … Carrizo, D. (2012). Large extensional aftershocks in the continental forearc triggered by the 2010 maule earthquake, chile. *Geophysical Journal International*, *188*(3), 879–890.

Salazar, K., & McNutt, M. (2011). Report on the 2010 chilean earthquake and tsunami response. *Reston, Virginia: US Geological Survey*.

Satriano, C. (2021). Sourcespec–earthquake source parameters from s-wave displacement spectra. *Zenodo*.

Scholz, C. H. (2015). On the stress dependence of the earthquake b value. *Geophysical Research Letters*, *42*(5), 1399–1402.

Schorlemmer, D., Wiemer, S., & Wyss, M. (2005). Variations in earthquake-size distribution across different stress regimes. *Nature*, *437*(7058), 539–542.

Sculley, D. (2010). Web-scale k-means clustering. In *Proceedings of the 19th international conference on world wide web* (pp. 1177–1178).

Shelly, D. R., Beroza, G. C., & Ide, S. (2007). Non-volcanic tremor and low-frequency earthquake swarms. *Nature*, *446*(7133), 305–307.

Skoumal, R. J., Brudzinski, M. R., Currie, B. S., & Levy, J. (2014). Optimizing multi-station earthquake template matching through re-examination of the youngstown, ohio, sequence. *Earth and Planetary Science Letters*, *405*, 274–280.

Steve Roecker, & Ray Russo. (2010). *Ramp response for 2010 chile earthquake.* International Federation of Digital Seismograph Networks. Retrieved from `https://www.fdsn.org/networks/detail/XY_2010/` doi: 10.7914/SN/XY_2010

Tan, Y. J., Waldhauser, F., Ellsworth, W. L., Zhang, M., Zhu, W., Michele, M., ... Segou, M. (2021). Machine-learning-based high-resolution earthquake catalog reveals how complex fault structures were activated during the 2016–2017 central italy sequence. *The Seismic Record*, *1*(1), 11–19.

Tassara, A., Soto, H., Bedford, J., Moreno, M., & Baez, J. C. (2016). Contrasting amount of fluids along the megathrust ruptured by the 2010 maule earthquake as revealed by a combined analysis of aftershocks and afterslip. *Tectonophysics*, *671*, 95–109.

Trugman, D. T., & Shearer, P. M. (2017). Growclust: A hierarchical clustering algorithm for relative earthquake relocation, with application to the spanish springs and sheldon, nevada, earthquake sequences. *Seismological Research Letters*, *88*(2A), 379–391.

van der Elst, N. J. (2021). B-positive: A robust estimator of aftershock magnitude distribution in transiently incomplete catalogs. *Journal of Geophysical Research: Solid Earth*, *126*(2), e2020JB021027.

Vigny, C., Socquet, A., Peyrat, S., Ruegg, J.-C., Métois, M., Madariaga, R., ... et al. (2011). The 2010 m w 8.8 maule megathrust earthquake of central chile, monitored by gps. *Science*, *332*(6036), 1417–1421.

Vilotte, J., & et al. (2011). Seismic network xs: Chile maule aftershock temporary experiment (resif-sismob). *RESIF-Réseau Sismologique et géodésique Français*.

Waldhauser, F. (2001). hypodd—a program to compute double-difference hypocenter locations (hypodd version 1.0-03/2001). *US Geol. Surv. Open File Rep., 01*, *113*.

White, M. C., Fang, H., Nakata, N., & Ben-Zion, Y. (2020). Pykonal: a python package for solving the eikonal equation in spherical and cartesian coordinates using the fast marching method. *Seismological Research Letters*, *91*(4), 2378–2389.

Yao, D., Walter, J. I., Meng, X., Hobbs, T. E., Peng, Z., Newman, A. V., ... Protti, M. (2017). Detailed spatiotemporal evolution of microseismicity and repeating earthquakes following the 2012 mw 7.6 nicoya earthquake. *Journal of Geophysical Research: Solid Earth*, *122*(1), 524–542.

Yue, H., Lay, T., Rivera, L., An, C., Vigny, C., Tong, X., & Baez Soto, J. C. (2014). Localized fault slip to the trench in the 2010 maule, chile mw= 8.8 earthquake from joint inversion of high-rate gps, teleseismic body waves, insar, campaign gps, and tsunami observations. *Journal of Geophysical Research: Solid Earth*, *119*(10), 7786–7804.

Zhu, W., & Beroza, G. C. (2019). Phasenet: a deep-neural-network-based seismic arrival-time picking method. *Geophysical Journal International*, *216*(1), 261–273.